國立交通大學

電子物理系

碩 士 論 文

銀和鉛薄膜在鍺(111)基底上的電子結構
的光電子能譜研究

Photoemission studies of the electronic structures of
Ag/Ge(111) and Pb/Ge(111)

研 究 生：邱鈺梅

指導教授：黃迪靖　教授

中 華 民 國 九 十 七 年 七 月

銀和鉛薄膜在鍺(111)基底上的電子結構的光電子能譜研究

Photoemission studies of the electronic structures of Ag/Ge(111) and Pb/Ge(111)

研 究 生：邱鈺梅　　　　　Student：Yu-Mei Chiu

指導教授：黃迪靖　　　　　Advisor：Di-Jing Huang

國 立 交 通 大 學

電子物理研究所

碩 士 論 文

A Thesis

Submitted to Department of Electrophysics

College of　Science

National Chiao Tung University

in Partial Fulfillment of the Requirements

for the Degree of Master

in Electrophysics

July 2008

Hsinchu, Taiwan, Republic of China

中華民國九十七年七月

銀和鉛薄膜在鍺(111)基底上的電子結構
的光電子能譜研究

學生：邱鈺梅　　　　　　　　　　　指導教授：黃迪靖 教授

國立交通大學電子物理研究所

摘　　　要

本論文中，我們利用光電子能譜研究銀和鉛薄膜在鍺(111)基板上的電子結構。在不同厚度時量測銀薄膜的表面電子態和量子井電子態，分析各量子數的量子井態在布里淵區中心的有效質量，我們發現隨著厚度的減少，布里淵區中心的有效質量會明顯變大。我們提出了一個模型來解釋所觀察到的現象，假設相位移與波向量的垂直和水平分量有關，從 Bohr-Sommefeld 量子化規則延伸，可得到量子井電子態在布里淵區中心的有效質量與薄膜厚度和相位移的關係式，我們從銀薄膜在鍺(111)系統得到的實驗結果，可用來驗證我們所提出的模型。

鉛在鍺(111)基板上形成表面重構，觀察其電子結構，我們發現在低溫時，電子結構與室溫時大致相同，但是會出現一個新的表面電子態，能量靠近費米能階，電子結構的改變暗示著從室溫到低溫的過程可能伴隨著原子結構的改變。此外，我們所量測到的表面電子態，在布里淵區中心附近展現出鍺的價帶邊緣，包含自旋─軌道交互作用所形成的重電洞、輕電洞和裂帶電洞能帶和沒有自旋─軌道交互作用所形成的三重結構，我們推測當鉛原子在鍺表面形成重構時產生的表面電子態會造成鍺表面的能帶彎曲，使得表面電子態與晶體中的電子態交互作用，最後顯現出鍺的價帶邊緣結構。

Photoemission studies of the electronic structures of Ag/Ge(111) and Pb/Ge(111)

student：Yu-Mei Chiu

Advisors：Dr. Di-Jing Huang

Department（Institute）of Electrophysics
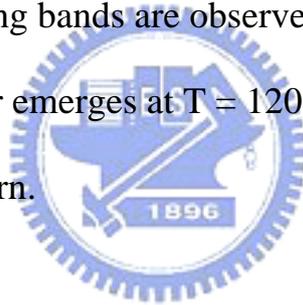National Chiao Tung University

ABSTRACT

The electronic structures of the ultrathin metal films on the semiconductor have been investigated by high resolution angle-resolved photoemission. In this thesis, the electronic structures of Ag/Ge(111) and of Pb/Ge(111) are studied. Ag/Ge(111) thin films are prepared at the thickness ranging 5-18 monolayers and the subband dispersions of quantum well states have been measured by angle-resolved photoemission. The enhanced effective masses of the subbands for decreasing film thickness have been observed in Ag/Ge(111) as well as in some other systems from previous studies. We find the in-plane effective mass at the zone center follows closely a trend as $1/N$ dependence where N is the number of the monolayer for thickness. This can be attributed to a kinetic constraint for standing wave formation governed by a

momentum-dependence phase shift function.

Pb/Ge(111) systems have been the center of interest . The electronic structures of the Pb/Ge(111) ($\sqrt{3} \times \sqrt{3}$)R30° reconstruction were reported. We made a Pb/Ge(111) ($\sqrt{3} \times \sqrt{3}$)R30° reconstruction surface from a   highly-doped n-type Ge(111),   and the   resulting band structures turned out to be quite different from those in the previous reports. Near the zone center, the surface state band dispersions reflect the valence band edges of Ge, including the heavy-hole, light-hole, and split-off hole bands. Both spin-orbit splitting bands and non-spin-orbital splitting bands are observed.   In addition, a new surface state band centered at k-bar emerges at T = 120 K while no phase transition is observed from LEED pattern.

Acknowledgment

Contents

Chapter 1

Introduction

As electronic device miniaturization descends further toward the atomic realm, quantum mechanical effects become important. Effects resulting from the confinement of electronic structure are called quantum size effects. The films are interesting in this regard as they are the basic of devices and have simple geometry to analysis. The films can exhibit an electronic structure markedly different from the bulk counterpart. When the thickness of the films decreases, the system can be considered as a quantum well and a quantization of the electronic structures perpendicular to the surface is observed. In a film $k_\perp$ is discrete while $k_\parallel$ is continuous. Quantum well states have a continuous dispersion transverse to the film; this band is called the subband. The in-plane subband dispersion is related to charge transport and other effects relevant to scientific and device applications.

The fundamental understanding of metal/semiconductor interfaces has been an important subject in surface science and film growth. Angel-resolved photoemission is a direct method to probe the band structure of solids. The knowledge of the electronic band structure of a solid is fundamental to the understanding of its physical properties.

In the following chapters, the background knowledge of the photoemission spectroscopy is introduced in chapter 2. Chapter 3 describes the basic concepts of the electronic states in thin films. Two systems, Ag/Ge(111) and Pb/Ge(111), are investigated in this thesis and are described in chapters 4 and 5, respectively. In chapter

4, the increased effective masses of the subbands at the zone center for decreasing films thickness are discussed. Chapter 5 describes the electronic structures of the submonolayer Pb film on highly-doped n-type Ge(111) surface. Finally, the results are summarized in chapter 6.

Chapter 2

Photoemission

2.1 Introduction

Photoemission spectroscopy (PES) is one of the important experimental techniques to measure the electronic structure of solid materials. The technique is based on the photoelectronic effect which was first observed in 1887 by Heinrich Hertz. In 1905, Albert Einstein explained the effect was caused by the absorption of "quanta of light", or "photon" in modern sense. An electron absorbs the energy of a photon; if its energy is sufficiently enough, it escapes from the material with finite kinetic energy.

The mean free path of an excited electron is generally short, typically a few angstroms, therefore photoemission did not become a common method until 60's with the advent of ultra high vacuum system. Figure 2.1 gives the mean free path λ as a function of their kinetic energy for various materials. λ is only the order of Å in the energy range between 10 to 2000 eV. Electrons with kinetic energy 20 - 100 eV having a short mean free path and generally penetrating only a few angstroms into the material are ideal probes for the surface.

Figure 2.2 exhibits the ingredients of the photoemission experiment. The light impinges on the sample and excites electrons. The light source can be either a gas discharge lamp or a synchrotron radiation source. When photons in the ultraviolet spectral range (0-100 eV) are used, the technique is called UPS (UV Photoemis-
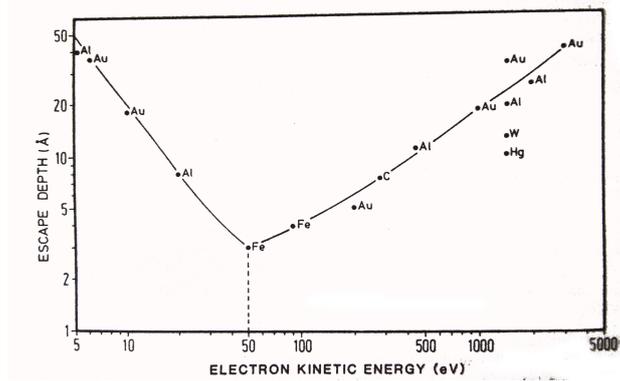
Figure 2.1: Electron mean free path as a function of their kinetic energy for various materials [1].

Figure 2.2: Sketch of a PES experiment. [1]

sion Spectroscopy) ; with X-ray radiation it is called XPS (X-ray Photoemission Spectroscopy) with photon energy > 1000 eV or SXPS (Soft X-ray Photoemission Spectroscopy) with photon energy   100 − 1000 eV. The kinetic energies E_{kin} and the wave vector **k** of the photoelectrons are detected by an energy analyzer.

4

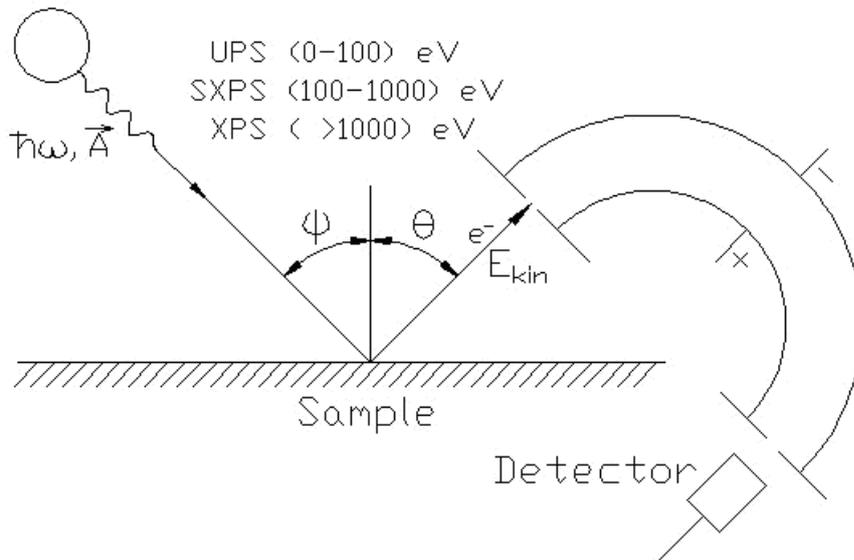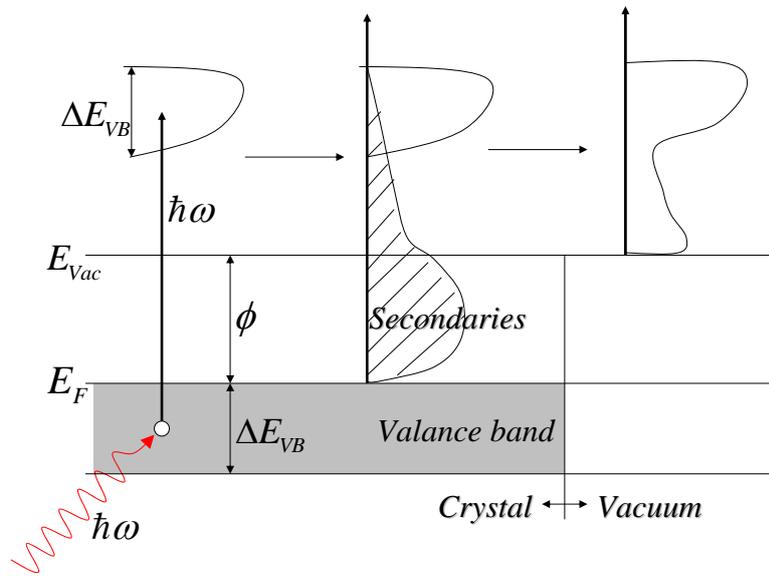Figure 2.3: Illustration of the three-step model in PES. The three-step model consists of (1) photoexcitation of an electron, (2) its travel to the surface and (3) its transmission through the surface into the vacuum.

2.2 The Photoemission Process

2.2.1 Three-step Model

The most commonly used model for the interpretation of photoemission spectra in solid is the so-called three-step model, as shown in Fig. 2.3. It is a purely phenomenological approach, which breaks up the complicated photoemission process into three steps [2] :

1. Optical excitation of an electron from an initial to a final state within the crystal.

2. Propagation of the excited electron.

3. Emission of the electron from the solid into vacuum.

Step 1 : Optical excitation of the electron in the solid.

Neglecting the momentum of the photon, the optical excitation is a direct transition in the reduced zone scheme. The internal energy distribution of photoexcited electrons $N_{int}(E, \hbar w)$, E being the final kinetic energy and $\hbar w$ the photon energy,

is given by

$$N_{int}(E, \hbar w) \propto \sum_{f,i} |M_{fi}(\mathbf{k}_i, \mathbf{k}_f)|^2 \, \delta \left(E_f(\mathbf{k}_f) - E_i(\mathbf{k}_i) - \hbar w \right) \delta \left(E - (E_f(\mathbf{k}_f)) \right) \quad (2.1)$$

where $E_f(\mathbf{k}_f)$ and $E_i(\mathbf{k}_i)$ denote the energy of the final and the initial states respectively. The first delta function imposes energy conservation during the first step while the second delta function ensures that the energy measured outside the sample equals the final state energy inside.

$|M_{fi}(\mathbf{k}_i, \mathbf{k}_f)|^2$ is the the square of transition matrix element of the interaction operator

$$H^{int} = \frac{1}{2mc} \left(\mathbf{A} \cdot \hat{\mathbf{p}} + \hat{\mathbf{p}} \cdot \mathbf{A} \right) \quad (2.2)$$

where $\mathbf{A}$ represents the vector potential of the incident electromagnetic field and $\hat{\mathbf{p}}$ is the momentum operator of the electron. The matrix element is evaluated by the Bloch waves of the initial and final states inside the crystal. In a first approximation direct transitions with nearly unchanged $\mathbf{k}$ are taken into account between the initial and final Bloch states, that is $\mathbf{k}_i \approx \mathbf{k}_f \approx \mathbf{k}$.

Step 2 : Transport of the electron to the surface.

During propagation, some photoexcited electrons may be scattered by plasmons, phonons or electrons and lose part of their kinetic energy. Such electrons contribute to the background in the photoemission spectra which is called the secondary background. They lose the information about their initial electronic level. The dominant scattering mechanism that reduces the number of photoexcited electron reaching the surface with E_f is the electron-electron interaction. The transport fraction of the total number of photoexcited electrons can be describe by a coefficient $d(E, \mathbf{k})$

$$d(E, \mathbf{k}) \simeq \frac{\alpha\lambda}{1 + \alpha\lambda} \quad (2.3)$$

where α is the optical absorption of light and λ the mean free path of electron. The mean free path is the average distance between collisions of two photoexcited electrons. Knowing that λ is much smaller than α^{-1}, one obtains $d(E, \mathbf{k}) \rightarrow \alpha\lambda$ which indicates the transportation without inelastic collision is proportional to the

mean free path.

Step 3 : Escape of the electron into vacuum.

The escaping electrons are those for which the component of the kinetic energy is sufficient to overcome the surface potential barrier; the other electrons are totally reflected back into the bulk. The transmission of the photoexcited electron penetrating the surface into the vacuum requires conservation of its wave vector component parallel to the surface:

$$\mathbf{k}_{\parallel}^{ex} = \mathbf{k}_{\parallel} + \mathbf{G}_{\parallel}; \tag{2.4}$$

where $\mathbf{k}_{\parallel}^{ex}$ and $\mathbf{k}_{\parallel}$ are the wave vector of the excited electron outside and inside the crystal respectively, and $\mathbf{G}_{\parallel}$ is the surface reciprocal lattice vector. Its normal component is not conserved since the translation symmetry is broken along the direction normal to the surface. $\mathbf{k}_{\perp}^{ex}$ is determined by the energy conservation requirement

$$E_{kin} = \frac{\hbar^2}{2m}\left[(\mathbf{k}_{\parallel}^{ex})^2 + (\mathbf{k}_{\perp}^{ex})^2\right] = E_F - E_{Vac}. \tag{2.5}$$

where E_F is the Fermi level and E_{Vac} is the vacuum level. With the work function $\phi = E_{Vac} - E_F$ and E_B as the binding energy referred to the Fermi level one has

$$\hbar\omega = E_f - E_i = E_{Kin} + \phi + E_B. \tag{2.6}$$

Transmission through the surface can be described by the transmission rate

$$T(E, \mathbf{k})\delta(\mathbf{k}_{\parallel} + \mathbf{G}_{\parallel} - \mathbf{k}_{\parallel}^{ex}). \tag{2.7}$$

Therefore, the formula for the external emission current in the three-step model writes

$$I_{int}(E, \hbar w, \mathbf{k}_{\parallel}^{ex}) \propto N_{int}(E, \hbar w)d(E, \mathbf{k})T(E, \mathbf{k})\delta(\mathbf{k}_{\parallel} + \mathbf{G}_{\parallel} - \mathbf{k}_{\parallel}^{ex}) \tag{2.8}$$

2.3 Angle-Resolved Photoemission

In angle-resolved photoemission spectroscopy (ARPES) the solid angle of the detector is small which allows exploitation of **k**-conservation by detection in a narrow **k**-interval. The parallel momentum is derived from the measured electron kinetic energy and its emission angle θ from the surface normal. For the photon excited

process both energy and momentum are conserved. With equation (2.4), $\mathbf{k}_\parallel^{ex}$ determined from the known experimental data,

$$\mathbf{k}_\parallel^{ex} = \sin\theta\sqrt{\frac{2m}{\hbar^2}(\hbar w - E_B - \phi)} = \sqrt{\frac{2m}{\hbar^2}E}\sin\theta \tag{2.9}$$

yields the internal wave vector component $\mathbf{k}_\parallel$. $\mathbf{k}_\perp^{ex}$ is determined according to (2.4) and (2.5) as

$$\mathbf{k}_\perp^{ex} = \sqrt{\frac{2m}{\hbar^2}E - (\mathbf{k}_\parallel + \mathbf{G}_\parallel)^2} = \sqrt{\frac{2m}{\hbar^2}E}\cos\theta. \tag{2.10}$$

However, no information of the $\mathbf{k}_\perp$ inside the crystal can be obtained without a detailed knowledge of electronic band structure for energies above vacuum level E_{Vac} and the inner potential. ARPES with high degree of angular resolution makes possible the experimental determination a dispersion relation $E(k_\parallel)$.

In our system, the energy analyzer and the photon beam are at fixed position. In order to detect the photoelectrons in different angles for some symmetric direction, the sample will be rotated to change the azimuthal angle. The definition of the parameters in an ARPES experiment are shown in Fig. 2.2, where θ is emission angle and φ is incident angle. As θ is changed, the angle between the surface and the light polarization is also changed. The intensity of peaks is proportion to the matrix element of the interaction operation, shown in (2.1). The intensity of the detected states is affected since the polarization of the light affects the photoemission cross section.

2.4 Photoemission Spectra

An energy distribution curve (EDC), consisting of a plot of the photoelectron count versus electron kinetic energy collected at a specific photon energy and emission angle, is dominated by a background, a sharp cutoff, and peaks, as shown as Fig. 2.4. All three primary features must be accounted simultaneously to accurately fit during analysis.
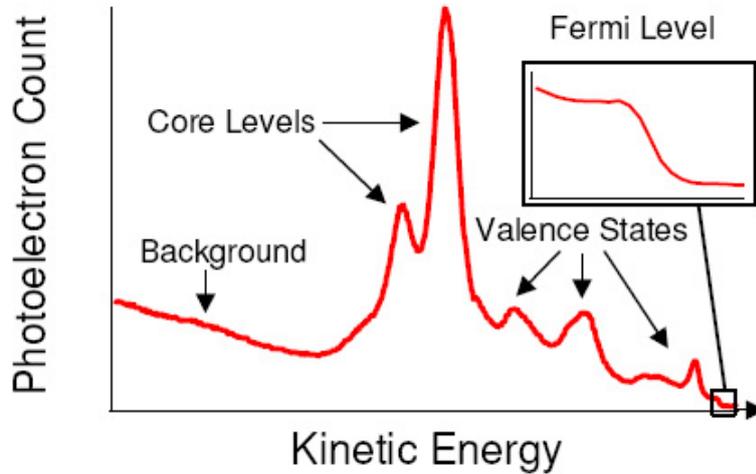
Figure 2.4: The schematic of the photoemission spectrum exhibits the typical features including background, Fermi level, and electron state peak.

The background arises from the inelastically scattered electrons. For valence spectroscopy the main contribution is a tail of secondary electrons. The background can be modeled as a polynomial function in electron energy.

The cutoff indicates where the Fermi level of the sample lies. It is not ideally sharp since the finite temperature effect cause a small number of counts populating the region above the Fermi level. With the standard Fermi function to fit the cutoff, the Fermi level E_F is determined in kinetic energy. Resetting the origin at the Fermi level, the photoemission spectrum can be scaled in terms of binding energy. When Fermi level falls in a semiconductor gap, no cutoff will be observed.

Occupied states, such as core level and valence states, appear as peaks. Core level states arise from electrons that are tightly bounded and appear at small kinetic energy. Valence states arise from electrons that are with weak bonding and close to the Fermi level.

ARPES is attractive in applications to quasi-2D materials since in this case direct and complete experimental determination of the band structure becomes possible. For 2D states like quantum well states or surface states, the final state effect can be

neglected, and the photoemission intensity measured in the detector change to be

$$I_v(E_{kin}, \mathbf{k}_\parallel) \propto \sum_{i,f} < f, \mathbf{k}_f | \widetilde{M}_{fi} | i, \mathbf{k}_i > \cdot A_h(\mathbf{k}, E) \qquad (2.11)$$

where $A_h(E)$ is the spectral function of the hole state which is in the form of a Lorentzian function

$$A_h(\mathbf{k}, E) = \frac{1}{\pi} \frac{|Im(\Sigma(\mathbf{k}, E))|}{[E - E_{\mathbf{k}}^0 - Re(\Sigma(\mathbf{k}, E))]^2 + [Im(\Sigma(\mathbf{k}, E))]^2}. \qquad (2.12)$$

$|Im(\Sigma(\mathbf{k}, E))|$ represents the linewidth of the initial hole state and is approximately given by

$$|Im(\Sigma(\mathbf{k}, E))| = \Gamma(E_B, T) = \Gamma_{def} + \Gamma_{e-p}(E_B, T) + 2\beta E_B^2 \qquad (2.13)$$

where E_B is the binding energy. The First term Γ_{def} which represents the contribution from defect scattering is independent of T and E_B. The second term which caused by phonon scattering is

$$\Gamma_{e-p}(E_B, T) = 2\pi\lambda \int_0^{E_D} \left(\frac{E'}{E_D}\right)^2 [1 - f(E_B - E') + 2b(E') + f(E_B + E')] \, dE' \qquad (2.14)$$

where the electron-phonon mass enhancement parameter λ enters as a proportionality constant, E_D is the Debye energy, and f and b are the Fermi-Dirac and Bose-Einstein distribution function, respectively. The third term is proportion to E_B^2 which is contributed from the electron-electron scattering.

ARPES is particularly suitable for studying many body interaction in 2D systems since it directly measures the spectral function of hole states given by (2.12). In practice, the peaks measured in experiment is broadened by thermal effects, sample disorder, and instrumental resolutions. The spectra are analyzed by fitting to a set of Voigt peaks superimposed on a smooth background function. The Voigt function is a convolution of a Lorentzian with a Gaussian function. The Lorentzian function accounts for lifetime broadening, which is given by

$$L(E, \Gamma) = \frac{\Gamma}{\pi} \frac{1}{E^2 + \Gamma^2}. \qquad (2.15)$$

The instrumental effects can be approximated by a Gaussian function,

$$G(E, \sigma) = \frac{1}{\sqrt{2\pi}\sigma} e^{-\frac{E^2}{2\sigma^2}} \tag{2.16}$$

Thus the formula for Voigt equation is

$$V(E, \sigma, \Gamma) = \int_{-\infty}^{\infty} L(E', \Gamma) G(E - E', \sigma) dE' \tag{2.17}$$

2.5 Ultra High Vacuum

From the experimental viewpoint, the preparation of a well-defined and clean surface, on which surface studies are usually performed, became possible only after the development of ultra high vacuum (UHV) techniques. UHV conditions are those with pressures below 10^{-9} torr. With a sticking coefficient $S = 1$, which means that every molecule or atom impinging on a surface sticks there, one needs an exposure of approximately 10^{-6} torr for one second to obtain a coverage of 1 monolayer on a surface. At a pressure of 10^{-10} torr it takes about 10000 seconds until a coverage of one monolayer is achieved. Fortunately, for many materials the sticking coefficients are much smaller than one. The preparation of well-defined surfaces with negligible contamination requires ambient pressures lower than 10^{-10} torr so that samples remain uncontaminated for several hours.

The process of lowering the pressure of a chamber from atmospheric pressure, 760 torr, down to the UHV regime requires different pumping mechanisms. A turbo-molecular pump starting in the 10^{-3} torr range which are established by a roughing pump is used to lower the pressure in the chamber down to 10^{-7} torr. Then a ion pump is turn on to pump down the the pressure to 10^{-9} torr. The pressure could not be lower since some molecules, mainly water molecules, adsorbed in the inner wall of the chamber would desorb slowly. To remove the molecules the process of bake is necessary.

The chamber is warned by several heating tapes and then covered with aluminum foils to achieve uniform temperature. When the current is applied to the heating tapes, the chamber will be heated. Note that the baking temperature should be

achieved within half a day and each component has different limited baking temperature: 200° for ion pump, 180° for energy analyzer, and 150° for evaporator. The baking temperature of the main chamber is keep at 150° and other component are keep at different temperatures to avoid possible damage to the accessories and instruments. Usually it takes two days to bake in our chamber to achieve a UHV condition. The degassing procedure should be carried out after bakeout. The chamber will be cooled after half a day and the pressure will be down to 5×10^{-10} torr or better.

2.6　Sources of Photons

Photoemission requires a high-intensity and monochromatic photon source. Helium lamps, laser system, X-ray tubes or synchrotron are usually used today, while helium lamps and laser systems are both lab-based source. The energy emitted by Helium lamp are at 21.2 and 40.8 eV. A number of groups are developing laser systems for low photon energy either tunable or not [4]. Yet X-ray tubes produce high energy photons , on the order of 1500 eV, which are used for core level spectroscopy for determining the composition of a material. They are not well suited to valence band studies. Synchrotron source is bright and photon energy is tunable, but the disadvantage is the limited beamtime. In our experiment, the sources are basically provided by Helium lamps and synchrotron radiations which are introduced by the following sections.

2.6.1　Helium Lamp

The operation of the high intensity VUV Source HIS 13 lamp is based on the principle of a cold cathode capillary discharge. When the potential applied between the ends of an insulating tube filled with gas is large enough, spontaneous breaking through occurs leading to a continuous discharge. The ignition potential is larger than the operating potential to maintain a continuous discharge.

The nature and intensity are strongly dependent on gas pressure and discharge current [3]. The optimum operational pressure of the lamps for the desired reso-
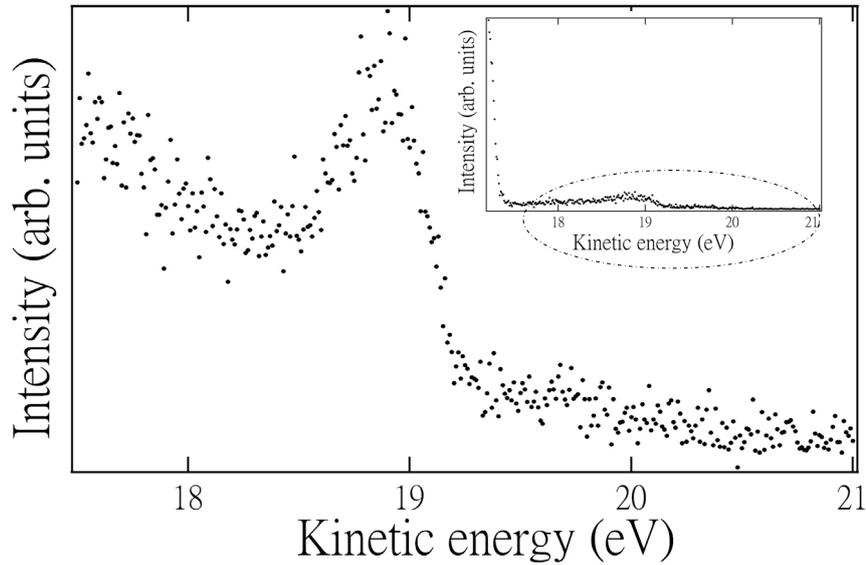
Figure 2.5: Comparing to the photon energy of He I α, the photoemission intensity induced by photon energy He II is weak. Choosing the region that no electron state induced by He I, as shown in the bottom picture, the electron excited by He II is observed at 18.83 eV..

nance line has to be determined experimentally. Studies by G. Schönhense and U. Heinzmann showed that the photon flux of the windowless lamp, which is differentially pumped, is dependent on the discharge current and operation pressure. For the resonance lines of the neutral atoms, such as He I, Ne I, Ar I, Kr I, Xe I, the optimum operation pressure shows a flat maximum. The photon flux vs. discharge current shows a saturation characteristic. For the resonance lines of the ionized gases, such as He II, Ne II, Ar II, Kr II, Xe II, the photon flux is proportional to the discharge current. Photons yield strongly increases with decreasing pressure.

In this experiment, the He gas is used to provide two different photon energies, He I and He II. The photon energy provide by He gases is shown in table 2.1. The main photon energy provided by He is 21.22 eV, He I α. Other photon energies exist but have weak intensity.

The photon energy of He II is also adopted in many experiments. As shown in

13

Table 2.1: Positions and intensities of He cold cathode discharge lines.

Source	Energy [eV]	rel. Intensity
He I α	21.22	100
He I β	23.09	1.2
He I γ	23.74	0.5
He II α	40.81	100
He II β	48.37	< 10
He II γ	51.02	n.a.

Fig. 2.5, the intensity of the kinetic energy below 17.3eV caused by the He I α is stronger. Crossing the Fermi edge, some signals emerge. At the kinetic energy 18.83 eV, a small peak appears which is corresponding to one of the Pb $5d_{5/2}$ core level. The work function of Pb(111) were measured to be 3.8 eV [5]. By (2.6), the kinetic energy of electron emission from $5d_{5/2}$ core level, with binding energies 17.9 and 20.6 eV [5], is equal to $40.81 - 3.8 - 17.9 = 19.11$ and $40.81 - 3.8 - 20.6 = 16.41$ eV , respectively. Which is consistent with our experiment data, a peak position at 18.83 eV. Yet another core level with binding energy 20.6 eV is not observed since its intensity is covered by the signal caused by He I. If the observed kinetic energy is lager than the Fermi energy corresponding to He I, the photon energy of He II is also another choice to use.

2.6.2 Synchrotron Radiation

Some of our data were taken at BL21B1 in National Synchrotron Radiation Research Center (NSRRC). This beamline is an undulator beamline with high flux and high resolution. Synchrotron radiation is light emitted by the electrons undergoing centripetal acceleration according to EM mechanics. Synchrotron facilities feature a storage ring where the electrons is bent into a quasi-circular trajectory by magnetic fields. When electrons are accelerated to travel a nonlinear course, they emit electromagnetic radiation. Under non-relativistic conditions, the radiation will adhere to a dipole distribution around the electron, as shown in Fig. 2.6. Whenever electrons moving close to the speed of light, $\beta \sim 1$, are deflected by a magnetic field, the radiation converges into a thin beam of radiation tangentially from their path
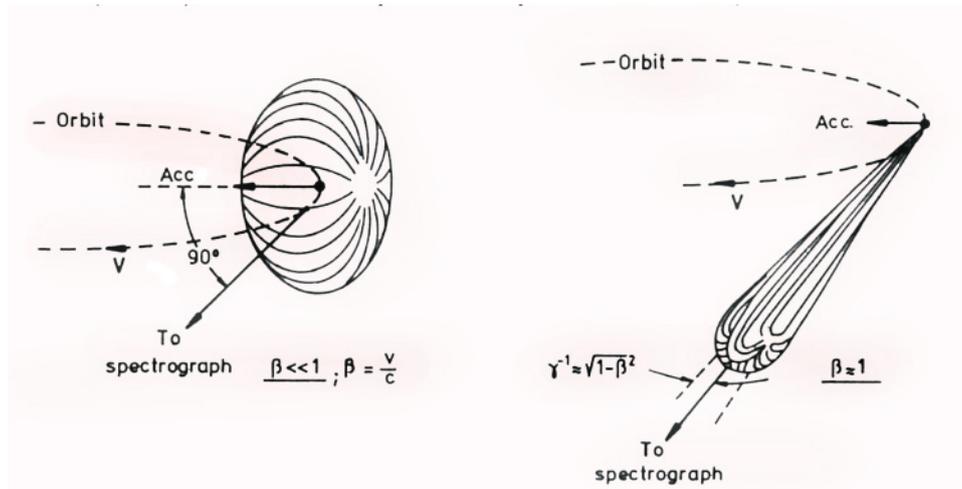
Figure 2.6: The angular distribution of the produced by electrons undergoing synchrotron radiation emission for non-relativistic and relativistic case. The radiation will adhere to a dipole distribution around the electron in the non-relativistic case; the photon is peaked sharply in the direction tangent to the circular path of the electrons in the relativistic case [1].

due to Lorentz transformation (effect).

In NSRRC, the electrons are first accelerated in the linear accelerator (LINAC) that boosts the electrons up to an energy of 50 MeV, and the booster ring then accelerates the electrons to an energy of 1.5 GeV. The electrons traveling at 99.999995 percent of the speed of light are then guided through a 70-meter-long transport line and into the storage ring, where electrons with an energy of 1.5 GeV circulate in an ultra-high-vacuum chamber for several hours. A series of magnets situated around the ring steer the electrons along circular arcs, and synchrotron radiation is continuously emitted tangentially from the arcs. The emitted light is channeled by the insertion devices through beamlines to the experimental stations where experiments are conducted [6].

Insertion devices (wigglers and undulators) comprising rows of magnets with alternating polarity produce brighter synchrotron radiation by causing the beam to oscillate rapidly. Wigglers cause multiple direction changes in the electron beam that generate extremely bright white light with short wavelengths; undulators cause periodic changes in the electron beam's direction that produce ultra-brilliant, single-

wavelength radiation from the resulting interference patterns.

2.7 Energy Analyzer

2.7.1 Electron Detector

SCIENTA 200 is equipped at BL21B1 and SCIENTA R3000 is equipped in our chamber. The main difference is the energy resolution due to the radius of the hemispherical analyzer and the function of them is the same. Only SCIENTA R3000 is introduced since it is similar to SCIENTA 200 and the energy resolution is test in our chamber.

SCIENTA R3000 is a high-resolution energy analyzer for photoemission spectroscopy [7]. The schematic overview of the system parts are shown in Fig. 2.7. The electrical potentials applied to the SCIENTA R3000 may reach up to 1.5 kV by the high voltage unit. The personal computer provides instrument control, read-out and data management. The electron spectrometer consists of three major parts: electron lens, hemispherical analyzer and detector assembly with a CCD camera. The multi-element electron lens act as a focusing lens, which were used to collect and transfer electrons from sample to the slit of the hemispherical analyzer; that matches the initial kinetic energy ($E_{kinectic}$) of the emission electrons to the fixed pass energy (E_{pass}) as the electrons start to enter the hemispherical analyzer. That is,

$$E_{pass} = E_{kinetic} - eV_{retarding} \tag{2.18}$$

where $V_{retarding}$ is the retarding potential provided by the electric lens to slow down the electron. Electron trajectories are bent in a 180° radial electrostatic field in the analyzer with positive charged inner sphere and negative charged outer sphere, as shown as Fig. 2.8.

The pass energy is the kinetic energy of the electron at the center of the detected energy band when it passes through the hemispherical analyzer which also relies on the voltage difference between the inner and outer spheres. The relationship can
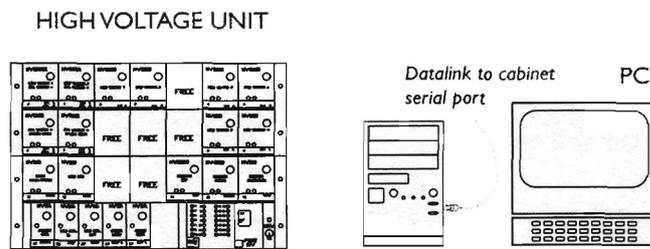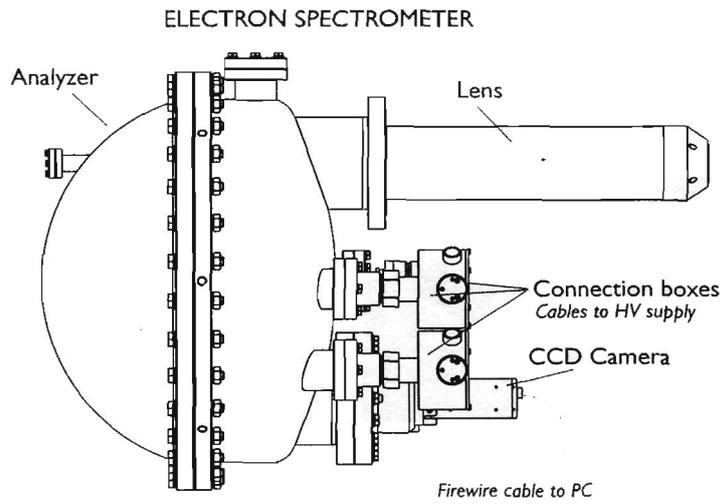
ELECTRON SPECTROMETER

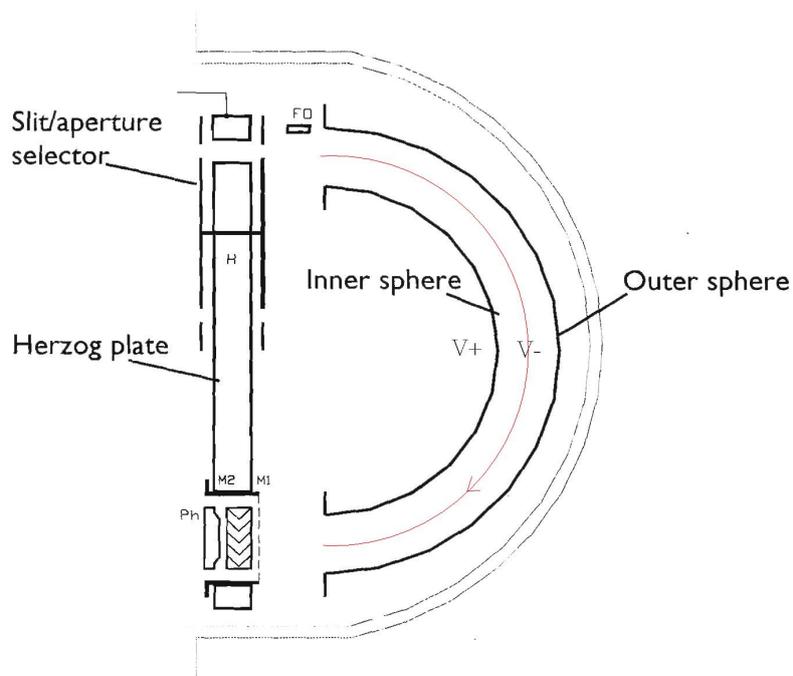Figure 2.7: The schematic overview of the SCIENTA R3000 system parts [7].

Figure 2.8: The schematic overview of the hemispherical analyzer [7].

describe as

$$E_{pass} = e\left(V_+ - V_-\right)\left(\frac{R_+ R_-}{R_-^2 - R_+^2}\right) \tag{2.19}$$

where $R_+(R_-)$ and $V_+(V_-)$ are the radius and voltage for inner (*outer*) sphere.

While the analyzer electric field ends at a field termination mesh, the Mulit-Channel Plates (MCP) pair multiplies each incoming electron about a million times. This electron pulse is accelerated to the phosphorous screen producing a light flash detectable by the FireWire CCD camera. The detector area registered by the CCD camera is a square of over 600 simultaneous energy channels and over 400 channels in the spatial or angular direction; that is, the MCP/CCD camera detection system is a 2-D detection system with energy in one direction and spatial or angular information in the other direction. It can determine their energy as well as the sample image or the electron emission angle simultaneously when the lens system were operated in transmission or angular multiplexing imaging modes.

In the transmission mode, the detector records the energy of all the electrons in a large angular range emitted from each location at a continuous range of positions on sample. Angular multiplexing mode is used for ARPES measurements, which efficiently probe the band structure of solids. In the angular mode, electrons emitted at identical angles are bind together, regardless of the position on the sample of emission, and the angular resolution will vary with the angular mode chosen.

The energy resolution of the electron spectrometer varies by the entrance slit size, shape, and the pass energy. Curved slits normally improve the energy resolution and straight slits achieve a higher count rate. The theoretical energy resolution is approximated with

$$\Delta E \approx \frac{sE_{pass}}{2R} \tag{2.20}$$

where s is the slit width and R is the analyzer radius. To achieve the best resolution a narrow curved slit, small pass energy and large analyzer radius should be used, whereas they give a lower intensity. With the MCP/CCD camera detection system the intensity scales approximately as $\sqrt{E_{pass}}$. As a rule of thumb high pass energy and small slit gives the best count rate.
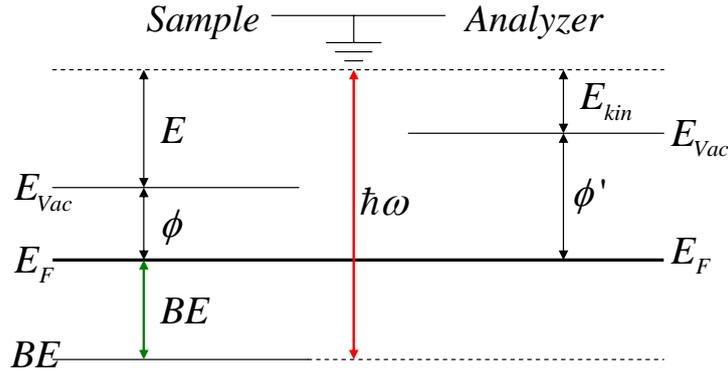
Figure 2.9: The sample and analyzer are grounded to ensure the kinetic energy E_{kin} measured in analyzer is the same as measured in sample.

The actual photoemission measurement is performed in an energy analyzer instead of vacuum. The kinetic energy E measured in vacuum and E_{kin} measured in an analyzer are not equal for the work function of sample and analyzer are different. In experiments, sample and analyzer are grounded to align their Fermi level to ensure that the binding energy $\hbar w - (E_{kin} + \phi')$ in analyzer is the same as $\hbar w - (E + \phi)$ in sample, shown in Fig. 2.9.

2.7.2 Resolution

The total energy resolution derives from the energy resolutions of the energy analyzer and of the incident photon beam, given by

$$\Delta E = \sqrt{\Delta E_{photons}^2 + \Delta E_{analyzer}^2}. \tag{2.21}$$

The energy resolution of analyzer is related to the pass energy and slit setting. As shown in (2.20), lower pass energy and narrow slit increase the energy resolution. SCIENTA R3000 is equipped with six slits, three curves and three straight slits. The table 2.2 shows the six different sets of slit-aperture pairs.

The resolution function can be measured at low temperatures. Fig. 2.10 gives a photoemission spectrum for the energy region around the Fermi energy. This figure depicts the spectrum measured for Mo and gives an analysis of the data by a Fermi

Table 2.2: Six modes of slit.

Mode	Width (mm)	Length (mm)	Shape
1	0.2	20	Straight
2	0.2	20	Curved
3	0.4	20	Curved
4	0.8	20	Curved
5	1.3	20	Straight
6	3.0	20	Straight

Table 2.3: The energy resolution with different modes of slit and pass energy.

Mode	Pass energy (eV)	ΔE (meV)
1	2	95.6
2	2	88.1
3	2	103.4
4	2	119.7
5	2	126.2
1	5	95.6
2	5	94.6
3	5	104.8
4	5	113.2
5	5	133.0

function convoluted with a Gaussian function. The solid line is the Fermi function at 120 K. The dashed line convoluted the Fermi function with a Gaussian of width 95.6 meV (FWHM), with pass energy 5 and slit mode 1. The full width at half maximum (FWHM) of the Gaussian function gives the energy resolution. For different pass energies and slits, ΔE are shown in table 2.3. It is not obvious that the lower pass energy and narrow slit increase the energy resolution. This may be caused by the large beam size.
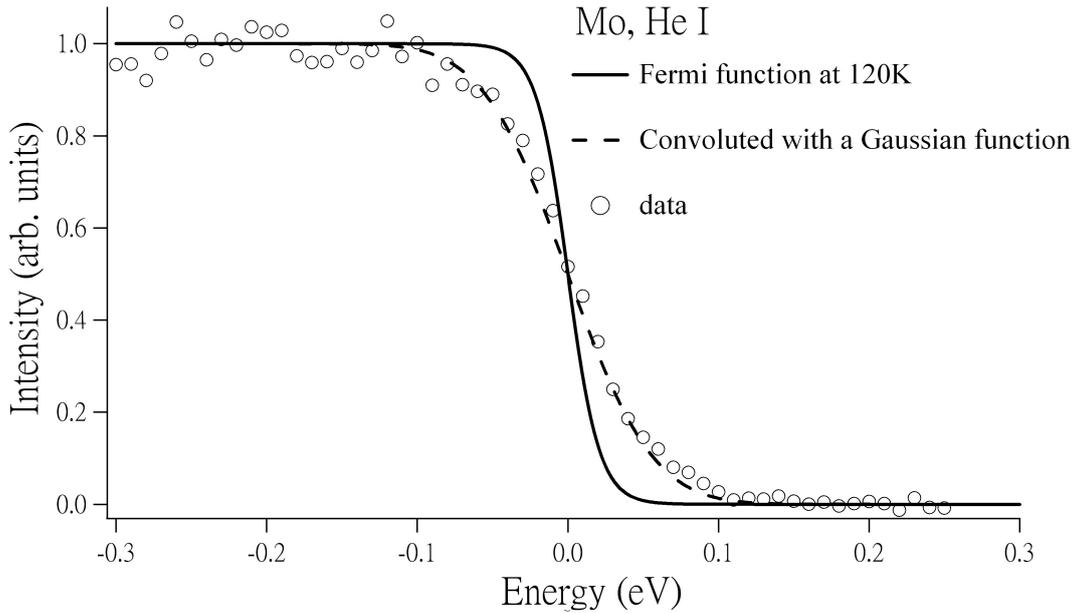
Figure 2.10: Energy distribution around Fermi level in photoemission spectrum from Mo at 120 K with photon energy 21.2 eV. The energy resolution is obtained by convoluting Fermi function (dashed line) with a Gaussian function of width 95.6 meV

2.8   Low Energy Electron Diffraction

Low energy electron diffraction (LEED) is a standard technique to check the crystallography quality of a surface, prepared either as a clean surface, or in connection with the ordered adsorbate overlayers. The LEED pattern exhibits sharp spots with high contrast on low background intensity. Defects or crystallographic imperfections will broaden the spots and increase the background. Electrons with energy between 10 and 200 eV incident on the surface and the elastically backscattered electrons give rise to diffraction spots that are imaged on a phosphorous screen. According to the de Broglie relation, the wavelength of electrons with kinetic energy E is given by

$$\lambda = \frac{h}{p} = \frac{h}{\sqrt{2mE}}, \qquad (2.22)$$

typically in the range of angstroms, where h is Planck's constant. For electrons with kinetic energy 20 eV the wavelength is about 2.7 Å. The low electron energy is suited for surface studies since the mean free path in the solid is short enough to give good surface sensitivity.
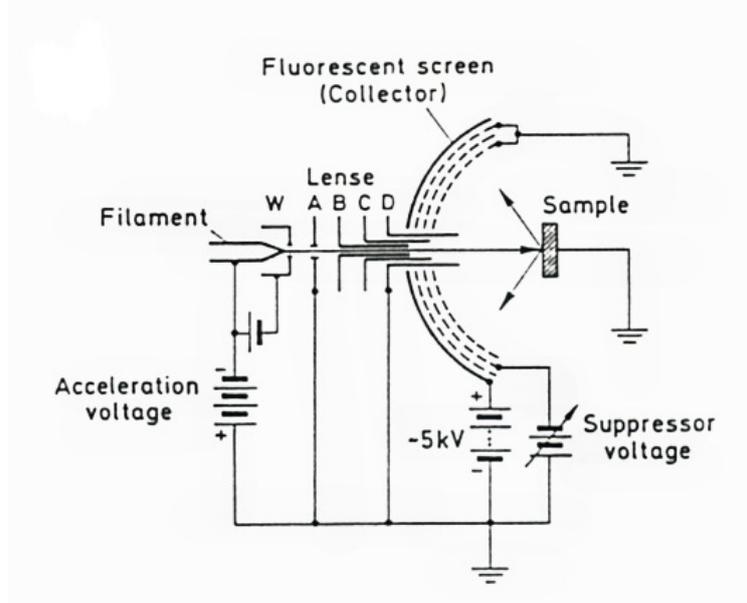
Figure 2.11: Schematic of a LEED optics for electron diffraction experiments [2].

The set up for LEED consists of an electron gun to produce an electron beam and the display system. A typical LEED system is exhibited in Fig. 2.11. Electrons emitted from a heated filament of the electron gun unit are accelerated by an electrostatic lens with apertures and incident normally on the sample. The low energy electrons are strongly backscattered by the electrons of the surface atoms.

Consider a one-dimensional chain of atoms with an electron beam incident normally into it. The interference maxima are in the direction given by

$$a \sin \theta = n\lambda \tag{2.23}$$

where a is the distance between the periodically arranged atoms, θ is the angle between normal and scattered electrons, and n is an integer number denoting the order of diffraction. This is a simple model for scattering of electrons by the atoms in the topmost layer of solid.

In the two-dimensional case, the condition for the occurrence of an elastic Bragg spot is given by

$$K_{\parallel} = k'_{\parallel} - k_{\parallel} = G_{\parallel} \tag{2.24}$$

where K is the scattering vector, k and k' are the wave vector before and after

scattering, and $G_\| = hg_1 + kg_2$ is the 2D surface reciprocal lattice. The wave vector before scattering is zero since the the electron beam hits the surface at normal incidence. This simplifies the analysis because the diffraction maxima can be directly associated with the reciprocal lattice and the diffraction pattern represents the symmetry of the surface. The diffraction pattern will be an image of the surface reciprocal lattice. The position of the intensity maxima on the fluorescent screen is described as

$$d_{h,k} = Rsin\theta_{h,k} = \frac{R}{|k'|}k'_\| = R\sqrt{\frac{\hbar^2}{2mE}}(hg_1 + kg_2), \qquad (2.25)$$

where R is the distance from the screen to the surface. The distance between reciprocal lattice points decreases with the increasing electron beam energy.

(a) 35eV

(d) 75eV

(b) 45eV

(e) 90eV

(c) 55eV

(f) 105eV
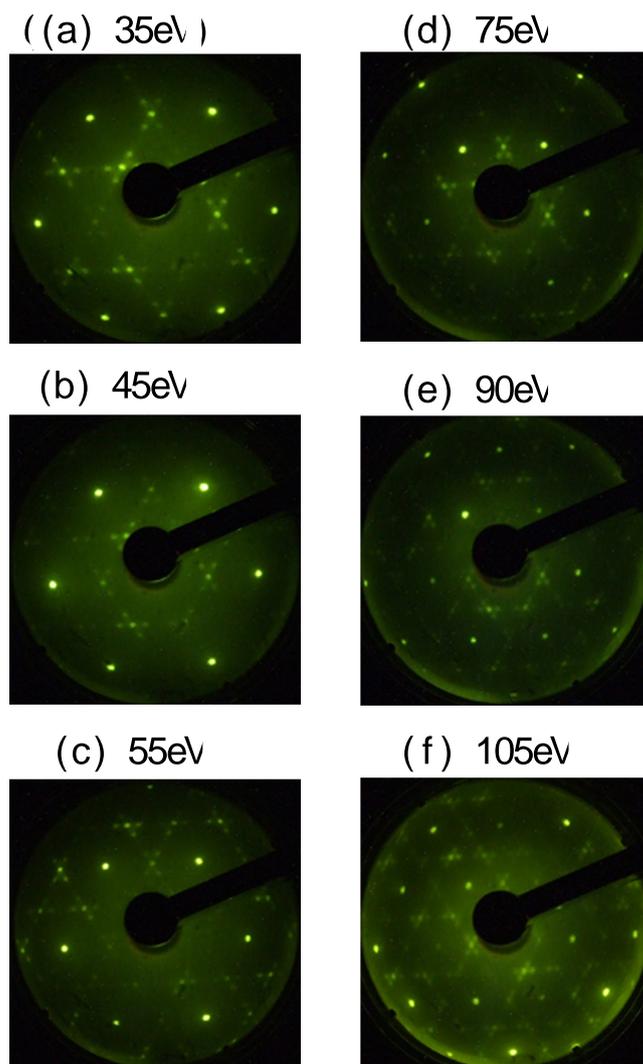
Figure 2.12: LEED patterns for clean Ge(111) surface with different electron energy.

Chapter 3

Surface Systems and Thin Films

3.1 Crystal Lattices and Surface Lattices

Pb and Ag have a face-centered cubic (fcc) lattice. The spacing between crystal plane depends on both the plane orientation and the particular crystal basis. For the simple fcc crystal with the lattice constant a, the cube diagonal spans four evenly-spaced planes and so adjacent (111) planes are separated by $a/\sqrt{3}$. The lattice constant of Pb and Ag are 4.95 Å and 4.09 Å, respectively. As it pertains to (111) film thickness, the spacing atomic planes between two adjacent is $a/\sqrt{3}$. As for Ag(111) film, one monolayer is equal to 2.36 Å; for Pb(111) film, it is equal to 2.86 Å.

A basis is the configuration of the individual constituents within a unit cell. The diamond structure is regarded as a face-centered cubic lattice with a two-point basis with one atom at the origin and the other located at the vector position $\mathbf{R} = (\hat{\mathbf{x}} + \hat{\mathbf{y}} + \hat{\mathbf{z}})/4$. The semiconductor Ge has a diamond structure crystal with lattice constant $a = 5.658$ Å. Successive planes are unevenly spaced along the cube diagonal with alternate separations of $\sqrt{3}a/12$ and $\sqrt{3}a/3$ as shown as Fig. 3.1.

3.1.1 Reciprocal Space

The real fcc lattices transform into body-centered cubic (bcc) lattices in k-space. The primitive unit cell about a reciprocal lattice point composed of a region of k-space that is closer to that point than to any other lattice point is termed the first
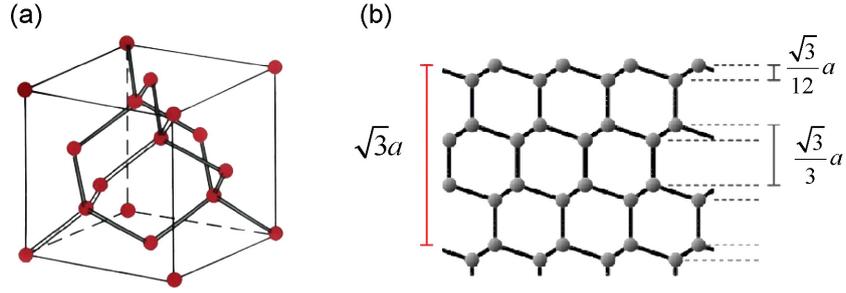
Figure 3.1: (a) The structure of diamond structure [8]. (b) Successive planes which are unevenly spaced along the cube diagonal produces a series of bilayer in the (111) orientation with alternate separations of $\sqrt{3}a/12$ and $\sqrt{3}a/4$.

Brillouin zone. The First Brillouin zone for a bulk *fcc* crystal is shown in Fig. 3.2, with high symmetry points and directions labeled by letters.

The electronic structure of a periodic solid can be described with band structure. The band calculation for Pb, Ag, and Ge are performed using the STATIC tight-binding code which is publicity available from the Naval Research laboratory and are presented in Fig. 3.3, where the electron energies as a function of wave vectors as are traversed along the high symmetry directions of the crystal Brillouin zone with the zero energy setting to the Fermi level.

3.1.2 Crystal Surfaces

In a real system, a crystal does not extend to infinity but rather possess a surface. The surface of a crystal depends on the particular plane that terminates the bulk lattice. For the (111) surface, the surface exhibits six-fold symmetry, as the set of $< 2\bar{1}\bar{1} >$ directions repeats at 60° intervals with the $< 1\bar{1}1 >$ directions offset by 30°.

The bulk termination of a crystal surfaces often produces an arrangement of atoms and bonds. To minimize the energy, the surface atoms configure into a stabilized reconstruction. The reconstruction is expressed in coordinates related to the periodicity of the underlying bulk terminated plane, specifically in reference to the
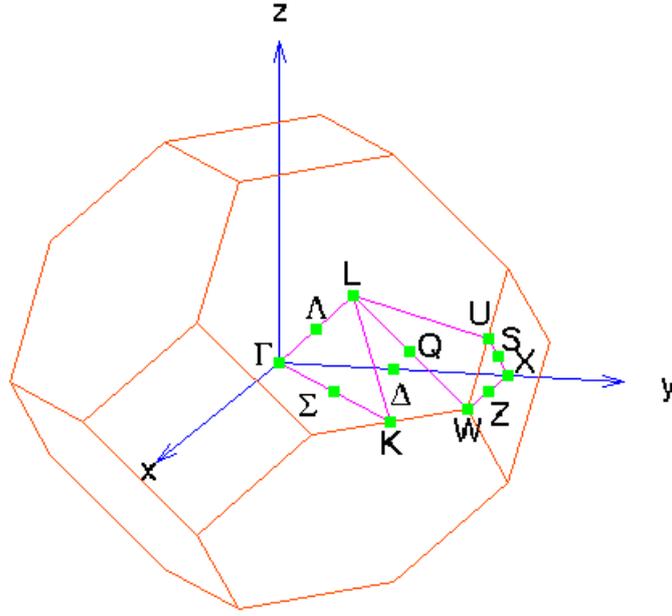
Figure 3.2: First Brillouin zone for a bulk fcc crystal [9].

1×1 unit surface cell. According to Wood there is a simple notation for reconstructions in terms of the ratio of the length of the primitive translation vectors of the reconstruction and the unit cell. The notation $N(n \times m)R\theta°$ denotes a reconstruction which has a periodicity of n bulk units by m bulk units rotated by θ degrees relative to the surface unit cell, where $N = p$ or c for primitive or centrad cells, respectively. One example of reconstruction is the Ge(111)-$c(2 \times 8)$ surface.

The interruption of a crystal lattice by finite boundary condition also alters its reciprocal lattice and the related electronic structure. The termination produces a 2D surface Brillouin zone (SBZ). The relation between the surface Brillouin zone and the bulk Brillouin zone for the fcc lattices is illustrated in Fig. 3.4, where the (111) surface Brillouin zone is the projection of the bulk Brillouin zone in the direction from Γ to L. The SBZ is a hexagon with the zone center denoted by $\bar{\Gamma}$, the zone boundary corner by $\bar{K}$, and the zone boundary edge by $\bar{M}$ and $\bar{M}'$. $\overline{\Gamma K}$ is parallel to $< 1\bar{1}0 >$ and $\bar{\Gamma}\bar{M}$ is parallel to $< 2\bar{1}\bar{1} >$.

Reconstruction can also be formed by depositing a small amount of atoms to surface, e.g. Pb on Ge. The Pb atoms on Ge substrates can form different ($\sqrt{3} \times$
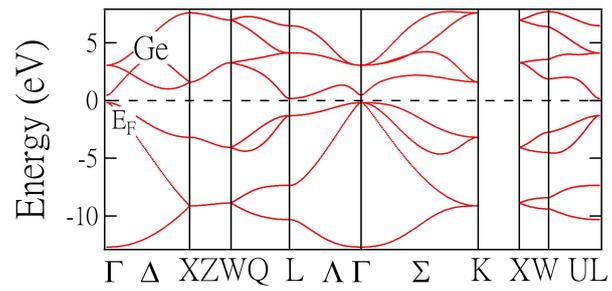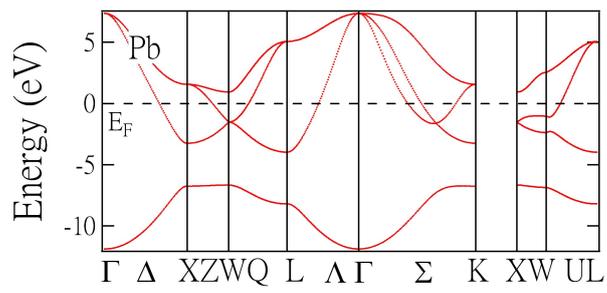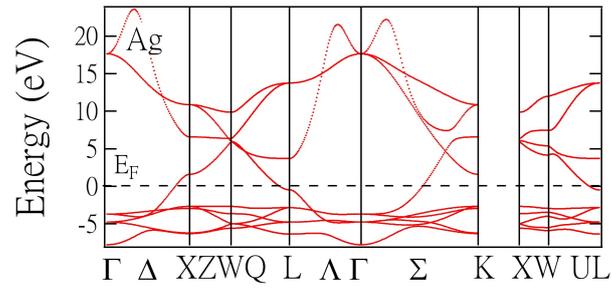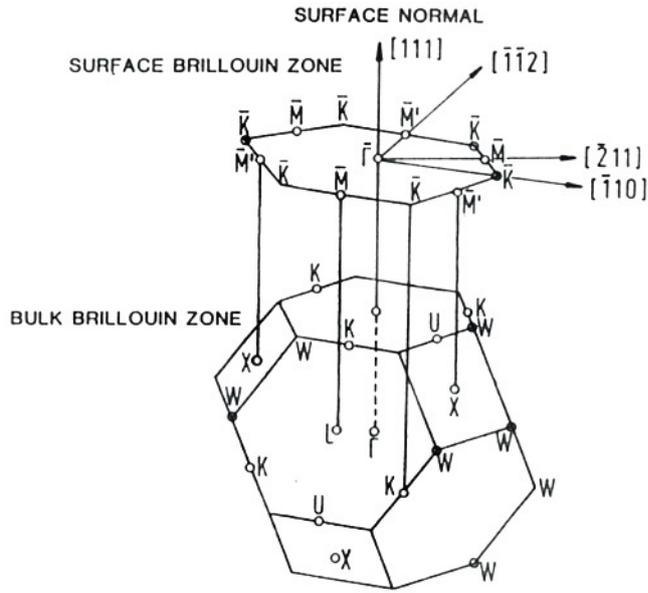
Figure 3.3: Band structures for Ag, Pb, and Ge.

28

Figure 3.4: Bulk and surface Brillouin zone for a *fcc* crystal [1].

$\sqrt{3})R30°$ reconstructions in the submonolayer regime. Early studies by Métois and Le Lay using low energy electron diffraction, Auger electron spectroscopy, and scanning electron microscopy found that the system exhibited the Stranski-Krastanov growth mode at room temperature [10, 11]. This is confirmed by Ichikawa using reflection high-energy diffraction [12, 13]. Métois and Le Lay found two different reconstructions with completion coverage of 1/3 and 1 monolayer (ML) in substrate units which were labeled by α and β phase, respectively. The coverage units used are referred to the Ge(111) unreconstructed substrate: 1 ML = 7.21×10^{14} atom/cm^2 = one-half of a Ge(111) double layer. Ichikawa found completion coverage of 2/3 and 4/3 ML for these phase. Later, more x-ray diffraction work and dynamical LEED I-V analysis found a completion coverage of 4/3 ML for β phase [14, 15]. In addition to the α and β phases, a completion coverage of 1/6 ML, labeled the γ phase, were found by T.-C. Chiang's group [16].

The general consensus is that the α phase is composed of 1/3 ML Pb atoms occupying the T_4 sites, as shown in Fig. 3.5 (a). T_4 sites are threefold-symmetric sites located directly above an atom in the second layer. In the 4/3 ML β phase, 1/3 Pb atoms are in H_3 sites and the remaining 1 ML Pb atoms are in bridge
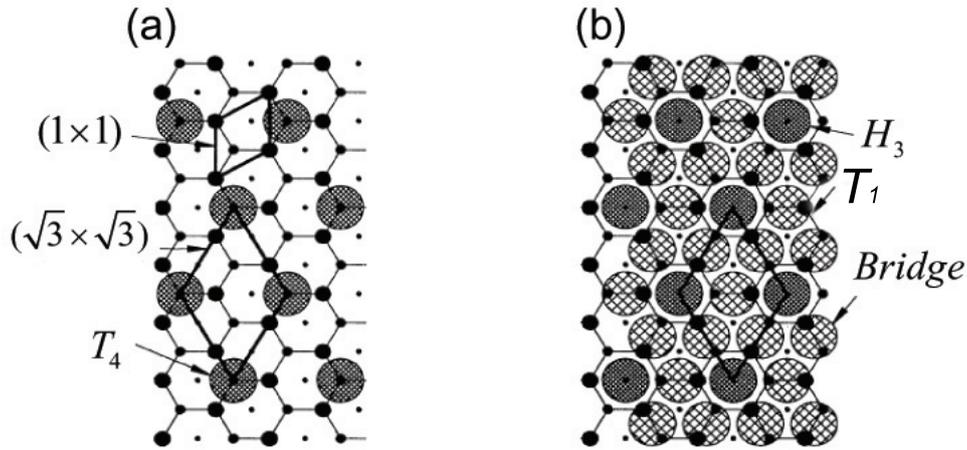
Figure 3.5: Structure models for the Pb/Ge(111) system. (a) α phase. (b) β phase [17].

sites, between T_1 and T_4 sites, as shown in Fig. 3.5 (b). This phase consists of a 1 percent compressed, close-packed Pb(111) layer rotated 30° with respect to the Ge substrate, namely, Pb$< 11\bar{2} > \parallel$ Ge$< \bar{1}10 >$. The occupied bridge sites between T_4 and T_1 sites with a small displacement to the T_1 sites are called off-centered (OC) T_1 sites [18]. Based on the previous photoemission and STM studies [19], the γ phase consists of an equal number of Pb and Ge adatoms on the surface, forming a mosaic phase. The structure model is similar to α phase but half Pb atoms are replaced by Ge atoms.

3.2 Surface Preparation

3.2.1 Clean Substrate

Sputtering of noble gas ion with subsequent annealing is the most general cleaning technique for metal surfaces and elemental semiconductors like Si and Ge. Contaminants are removed by bombardment with noble gas ions, and subsequent annealing can remove embedded and adsorbed noble gas so as to recover the surface crystallography. The ion current is produced by electron impact on noble gas atoms and accelerated by a voltage of few kilovolts towards the sample. The ion current, beam voltage, times of cycles, sputtering and annealing temperature all depend on the material and the thickness of the layer to remove. Sample heating can be done by
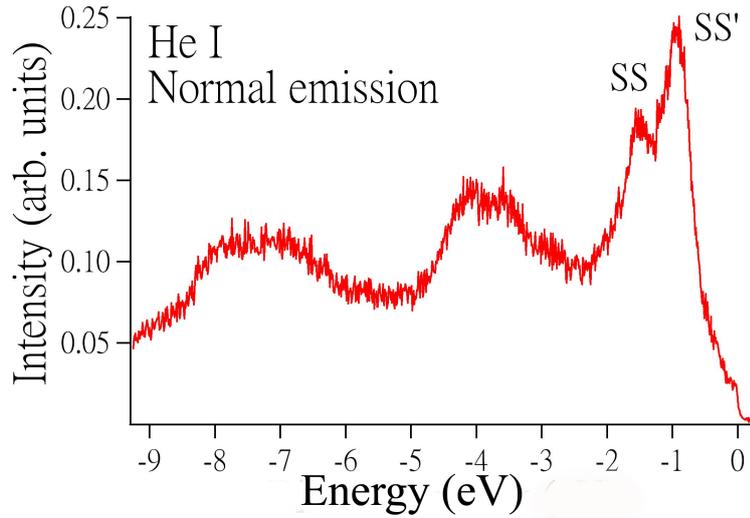
Figure 3.6: Photoemission spectroscopy of the clean Ge(111)-$c(2 \times 8)$ surface at normal emission.

resistance heating or electron bombardment heating (EBH).

A clean Ge(111)-$c(2 \times 8)$ surface was prepared by sputtering at a substrate temperature of $500°C$ followed by annealing at $600°C$. This procedure generally yields very sharp $c(2 \times 8)$ LEED pattern. Another way to check the cleanness of the surface is by the photoemission spectrum. As shown in Fig. 3.6, two sharp surface states labeled by SS and SS' are the indicator that the sample is clean [20, 21].

3.2.2 Film Growth

The deposited material can be developed into a film through layering or island coalescence. There are three growth modes: layer-by-layer, island, and layer-plus-island. The layer-by-layer (Frank-van der Merwe) growth mode occurs when the atoms of the evaporant are attracted strongly to the substrate than themselves. When the atoms are bound to each other strongly, islands will be formed. The layer- plus-island (Stranski-Krastanov) mode arises when the formation of a wetting layer is subsequently followed by island growth.

Recently a two-step growth method for thin film was widely used : a film is in growth at very low temperature and then anneal to suitable temperature [22]. At

low temperature the atoms are randomly distributed on the substrate to form disorder clusters. On annealing to a suitable temperature, the film will transform into an ordered, and atomically flat film.

Molecular beam epitaxy (MBE) is a standard technique for depositing a material onto a substrate. UHV EFM3 evaporator and K-cell evaporator are used in our chamber and beamline, respectively. In the EFM3, the evaporant is either evaporated from a rod or a crucible. This is achieved by electron bombardment heating. The bombarding electron beam induces a temperature rise of the evaporant and causes evaporation. The evaporation cell is enclosed in a water-cooled copper cylinder so that just a restricted region of the evaporant is heated. K-cell evaporator is equipped with a big crucible surrounded by a resistance heater.

The comparisons from two kinds of evaporators are described as following.

- The size of crucible for K-cell is larger than EFM3.

- The beam size of EFM3 is smaller.

- The depositing flux is more stable for EFM3.

- The preheating time for EFM3 is short.

3.2.3 Thickness of Thin Film

For higher coverage, one monolayer is defined as the spacing between crystal planes which depends on the plane orientation. For the simple fcc the adjacent (111) planes are separated by $a/\sqrt{3}$, where a is the lattice constant. When considering surface coverage under one monolayer, the conversion factor depends on both the substrate and the adsorbed materials and is given by

$$\Theta = \frac{\rho\,N_A}{W_M\delta_S}\,t = C\,t \tag{3.1}$$

where Θ is the thickness in monolayer, t is the thickness in angstrom, N_A is Avogadro's number, ρ and W_M are the density and molecular weight of the evaporant, δ_S is the site density of the substrate surface, and C is the surface factor.

The deposition rate can be determined by using a quartz-crystal thickness monitor. Usually, there is $10 \sim 20$ percents error of calibrating the thickness by thickness monitor. The quantum well electronic structure is sensitive to the thickness to the degree of one atomic layer. Thus the quantum well states can be used to monitor the roughness of the film and determine the thickness [23].

3.3   Surface States

Surface is the termination of a bulk crystal. Surface atoms have fewer neighbors than bulk atoms and some of the bonds are broken at surface. Therefore, the electric structure near the surface differs from bulk. Solving the Schrodinger equation for electrons roaming in the potential field which is periodic inside the crystal and constant in the vacuum region, the wave vector is then determined. When a crystal is limited by a surface, the restriction that k is real to ensure the wave function remains finite for an infinite crystal is no longer necessary. Bulk states are Bloch waves which oscillate in the solid and have a small tail into the vacuum. Additional surface solutions become possible if the wave vectors are complex. The wave function is localized near the surface and the energy falls into the forbidden gap of the projection of the bulk band and this is known as *surface state*, as shown in Fig. 3.7. The energy and parallel momentum of the surface state lie in a gap in the projection of the bulk band structure onto the SBZ. However surface states can penetrate into a part of the surface Brillouin zone, where propagating bulk states exist. Those states degenerated with bulk states and mixed with them are known as surface resonances and will propagate deep into the bulk.

The existence of the surface states can be easily explained by the picture of tightly bound electrons. For the top most atoms, they have fewer neighbors and their wave functions have less overlap with wave functions of neighboring atoms. The splitting and shifting of their energy levels are smaller than those in the bulk, as shown in Fig. 3.8.
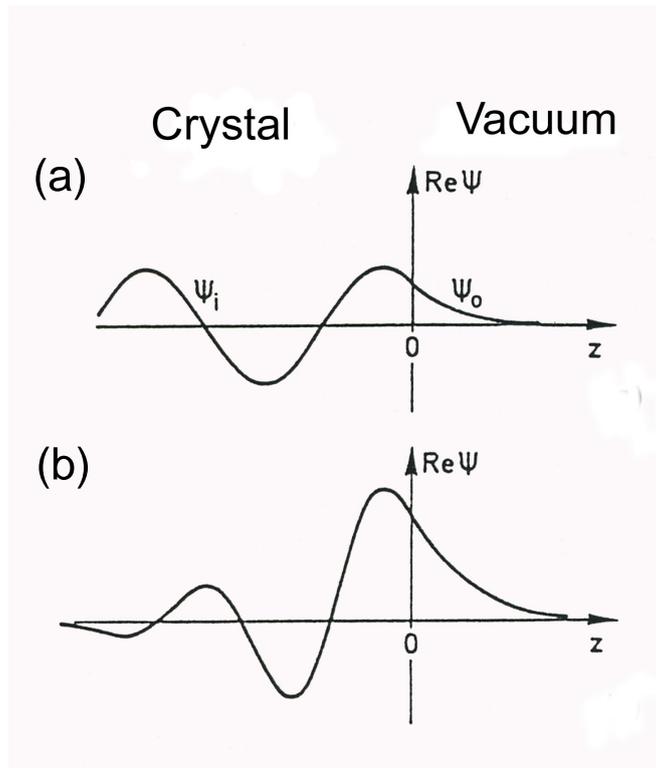
Figure 3.7: Wave function for (a) a standing Bloch wave and (b) a surface state [2].
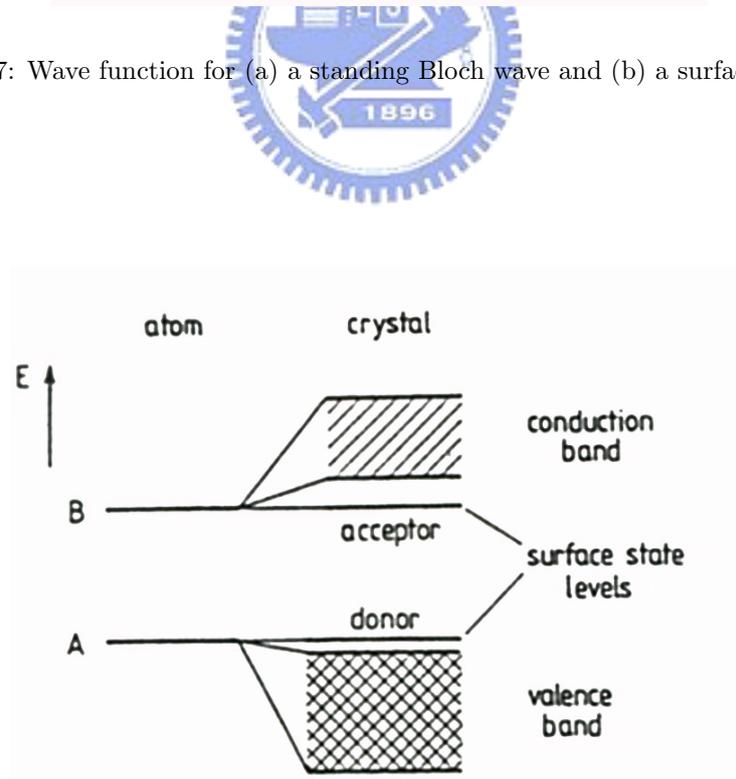

Figure 3.8: Surface states have acceptor-type or donor-type charging character [2].

The higher lying surface state has conduction band character whereas the lower level which is split off from the valence band of the semiconductor is more valence band like. The charging character of the surface states also reflects the corresponding bulk states. A semiconductor is neutral if all conduction band states are empty and all valence states are occupied. So the conduction band states carry a negative charge if they are occupied by an electron; the valence band states carry a positive charge when they are unoccupied. Surface states derived from the conduction band have the same characteristics, called acceptor-type states; surface states derived from the valence band have the same characteristic, called donor-type states.

Surface states can also be produced by adsorbed atoms which cause changes in the chemical bonds near the surface and affect the distribution of the intrinsic surface states. In addition, a new surface state can be formed by the bonding and antibonding orbitals between the adsorbed atoms and the surface. They form 2D lattices with translational symmetry along the surface and thus form the 2D band structures.
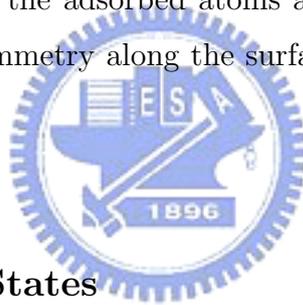
3.4 Quantum Well States

When electron states within the film overlap with the state in the substrate, no confinement will occur. However, if the electrons in film fall into the a band gap of the substrate, the electrons will be confined like particles-in-a-box, called quantum well states.. The width of the box is the thickness of the film. The electrons are confined between the film-vacuum and the film-substrate potential barriers. Confinement can be found in both metal-on-metal or metal-on-semiconductor system.

For the (111) thin films, the relevant direction in real space is the [111] direction, which is the surface normal for both the substrate and the film, corresponding to the ΓL direction in the k-space. Pb is a metal that displays a Fermi level band crossing. Ge is a semiconductor with a band gap in which the Fermi level falls. A comparison of the two band structures in Fig. 3.9 shows that the electrons with energy near
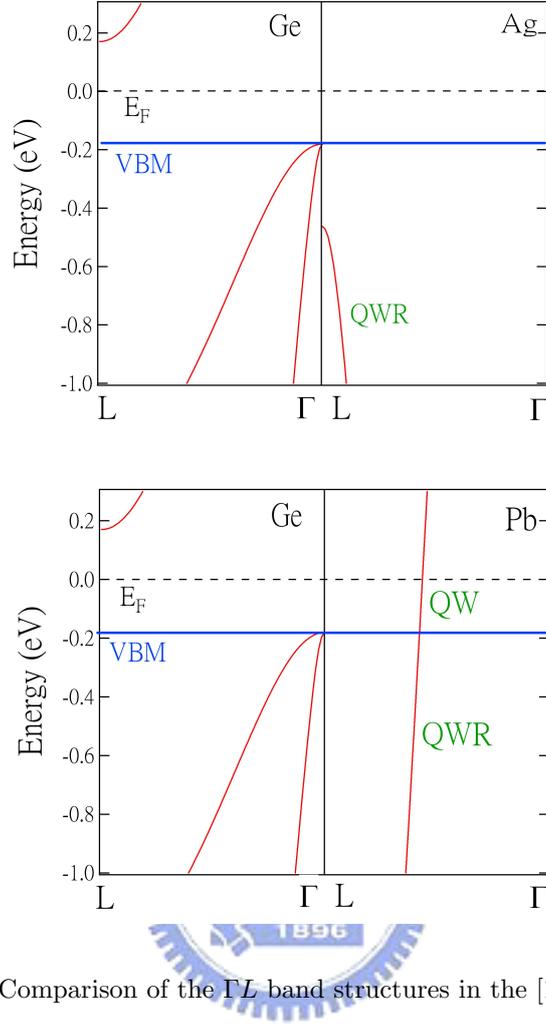
Figure 3.9: Comparison of the ΓL band structures in the [111] direction.

the Fermi level in Pb have no corresponding states in Ge above the valence band maximum (VBM) to which they can transit and thus they are confined in the film. Electrons in Pb with energy larger than VBM have corresponding states in Ge and they are not totally confined in the thin film. This is called quantum well resonance (QWR). For Ag/Ge(111) system, the metal electrons are not totally confined. All the states we observed at the zone center are quantum well resonance.

The electron state are only quantized in the direction perpendicular to the film, while the lateral expanse of the film is not restricted. As a confined electron traverses in the film, its wave function accumulates phase not only in the transit but also when it is reflected from the vacuum and substrate interface. The total phase accumulates to an integer multiple of 2π after the quantum well electrons make a round trip between two interfaces to form a standing wave like wave function. The quantum

well state energy level can be thus determined by the Bohr-Sommerfeld quantization rule, or phase accumulation model:

$$2k_\perp(E)Nt + \phi_i(E) + \phi_s(E) = 2n\pi \tag{3.2}$$

where $k_\perp$ is the electron wave vector perpendicular to the interface, E is the energy of the state, N is the number of the monolayer, t is the monolayer thickness, ϕ_i and ϕ_s are the energy dependent phase shift at the surface and interface, respectively; and n is a quantum number.

3.4.1   Quantum Number

In (3.2), one can choose to measure $k_\perp$ from the zone center (Γ point) or the zone boundary at the L point. The quantum numbers depend on where the origin is chosen. Conventionally the zone boundary is chosen as the origin. At the normal emission the wave vector is limited in the direction perpendicular to the surface while the parallel component of the wave vector is zero. The total phase in a round trip perpendicular to the surface is equal to an integer times 2π. The value of $k_\perp$ which satisfies (3.2) can be rewritten as

$$k_\perp = \frac{n\pi}{Nt} - \frac{\phi}{2Nt} \tag{3.3}$$

where $\phi = \phi_s + \phi_i$ is the total phase shift.

A film is invariant under a translation of t in the direction perpendicular to the surface, where t is the monolayer thickness. In the reciprocal lattice, the distance between the zone center and the zone boundary is equal to half of the reciprocal vector $\vec{\mathbf{G}} = \frac{2\pi}{t} = \Delta k_{\Gamma L \Gamma}$. The distance from the zone center to the zone boundary at L is π/t. When the phase shift is zero, the wave vectors satisfied (3.3) divide the region between the Γ and L point into N parts. For this simple case the allowed $k_\perp$ values are the integer times π/Nt. Thus the quantum number is labeled from 0 to N for N monolayers thin film. The wave vector corresponding to state $n = 0$ is at the zone center and the state $n = N$ is at the zone boundary. This should be the simplest case but is generally not real. The phase shift is due to the finite potential barrier at the film-vacuum surface and film-substrate interface and its value varies
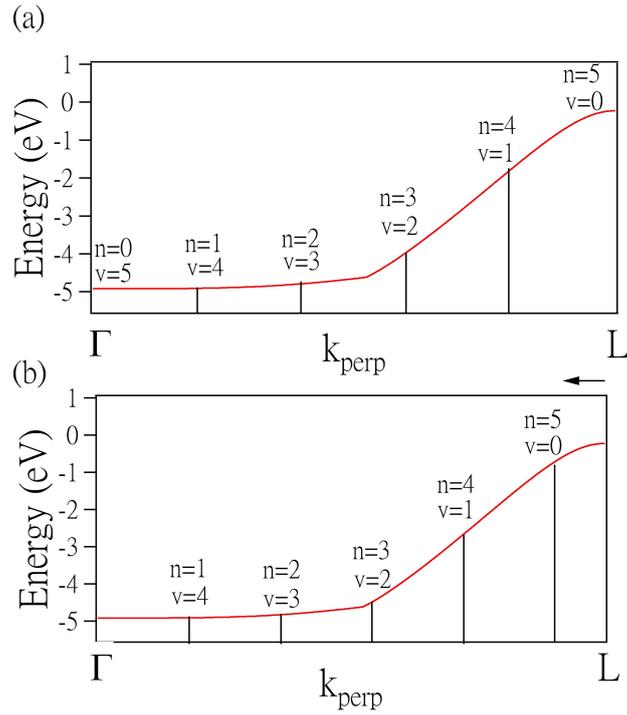
37

Figure 3.10: When the k value is measured from the band zone center Γ, the quantum numbers are denoted by n. When k is measured from L point, v is used. (a) The quantum numbers are labeled for zero phase shift. (b) For positive phase shift the allowed k values are shifted to the zone center.

from 0 to 2π. When the phase shift is put into consideration, the allowed wave vectors corresponding to the quantum well states will shift. For the positive phase shift, the allowed $k_\perp$ is shift toward the Γ point so that the corresponding quantum number n starts from 1 to N since the state $n = 0$ is out of the ΓL region. For the negative phase shift vice versa. Sometimes, for the sake of explicit expression, the quantum number $\nu = N - n$ is used if the quantum well states observed are near the zone boundary.

Figure 3.10(a) shows the allowed k, labeled both by n and v, for 5-ML Ag film when the phase shift is zero. The solid curve represents the Ag band structure in the [111] direction. As the phase shift becomes positive, the quantum number n starts from 1 to N and the allowed k values are shifted to the zone center, as shown in Fig. 3.10 (b).

Chapter 4

Ag Films on Ge(111)

4.1 Introduction

The increased effective masses of the subbands at the zone center for decreasing film thickness has been observed in other systems, such as Ag/V(100) [24], Cu/Co/Cu(001) [25, 26], and Pb/Si(111) [27].

Johnson *at al.* proposed that the large increases in effective mass of quantum well state electrons are due to the hybridization effect at the interface [26]. As the film thickness decreases, the dispersions are strongly influenced by the effect, as presented in Fig. 4.1 (a).

Dil *et al.* observed that the magnitude of in-plane effective mass in the Pb on Si(111) system is larger than those from bulk state or predicted by slab calculation, as shown in Fig. 4.1 (b) [28]. Having excluded an influence of the interface and substrate bands that might lead to the unusual band dispersion, a higher degree in-plane localization of the electron states in the Pb quantum wells are considered. This agrees with the recent suggestions from scanning tunneling microscopy studies that the Si(111) 7×7 reconstruction can be imaged through Pb layers of more than 100Å [29].

The Ag films on Ge(111) were well studied. The reasons why Ag is chosen as thin film and Ge(111) as the substrate are as follows: (1) Ag and Ge do not
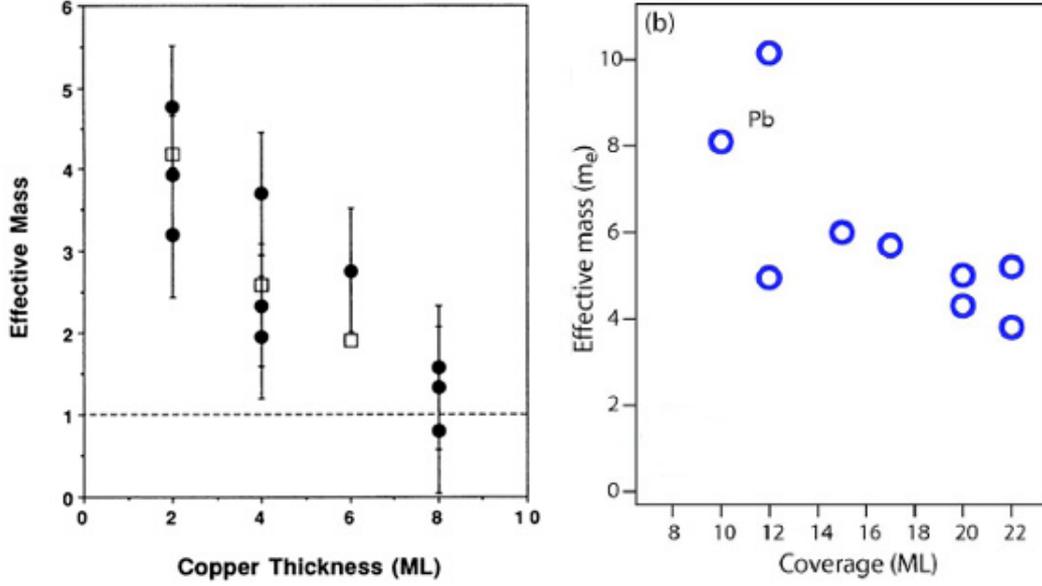
Figure 4.1: The in-plane effective mass versus the film thickness for (a) Cu/Co/Cu(001) [26] and (b) Pb/Si(111). [25]

intermix; (2) Ag only is a simple metal, a s-p metal, and the valence electrons are easy to analyze; (3) Ge is a well-known semiconductor. To deposit the amount of Ag accurately, Ag films ranging in thickness 5-18 monolayers are performed. The effective mass increasing with film thickness is also observed in this system. This phenomenon is merely a result of a extended Bohr-Sommerfeld quantization rule with a momentum-dependent phase shift.

4.2 Experiment

Ag was deposited onto the substrate using K-cell at a substrate temperature of 50 K. The sample was subsequently annealed at 300 K and cooled down to 50 K for measurement. The resulting Ag film was oriented along [111] with the crystallographic direction parallel to the same in the substrate. Photoemission spectra were taken as two dimensional images with the kinetic energy and the emission angle. Rotating the sample to change the detected emission angle, the surface electronic structure can be probed from the zone center $\bar{\Gamma}$ to the SBZ boundary. The dispersion relation direction is recorded along $\bar{\Gamma}\bar{M}$ direction with photons of energy 50 eV
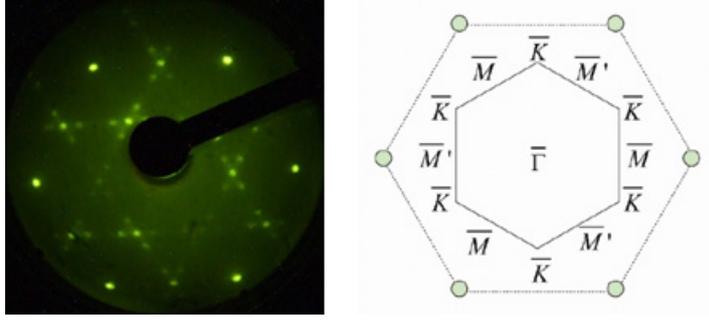
Figure 4.2: LEED pattern of clean Ge(111) surface and its corresponding surface Brillouin zone (solid).

and the direction was calibrated by LEED pattern. The Ge(111) LEED pattern and its corresponding SBZ are shown in Fig. 4.2.

The growth rate, about 0.4 ML per minute, was monitored by a quartz thickness monitor. The actual amount of Ag was determined by the evolution of quantum well states as a function of film thickness.

4.3 Results

The EDC's at normal emission for Ag thin films at the thickness from 5-ML to 18-ML are shown in Fig. 4.3. Peak SS is a surface state of Ag(111). This state has a long tail, and its interaction with the substrate at small thin thickness accounts for the complicated lineshape. Each QWS peak, labeled by quantum number $\nu = 1-5$, moves toward the Fermi level as the film thickness increases.

The quantum well states in Ag/Ge(111) system do not disperse like free electrons since the quantum well peaks split into two with an appearance resembling a two level anti-crossing as crossing the Ge bulk band edge. The ARPES data for $N = 6$ ML is shown in Fig. 4.4. This effect is more evident near the upper band edge.

The solid curve in Fig. 4.4 is a fit to the $\nu = 1$ subband dispersion relation using the model function:
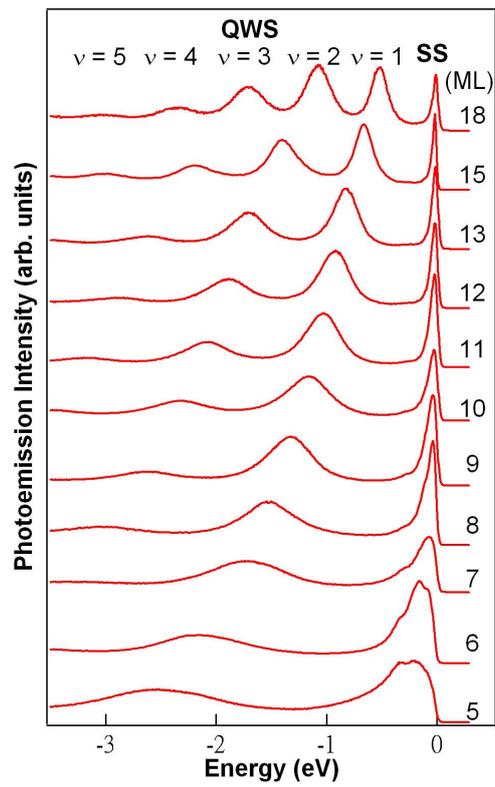
Figure 4.3: Energy distribution curves at normal emission for different thickness thin films. SS denotes a Surface state and QWS denotes the quantum well resonance states labeled by quantum number ν.
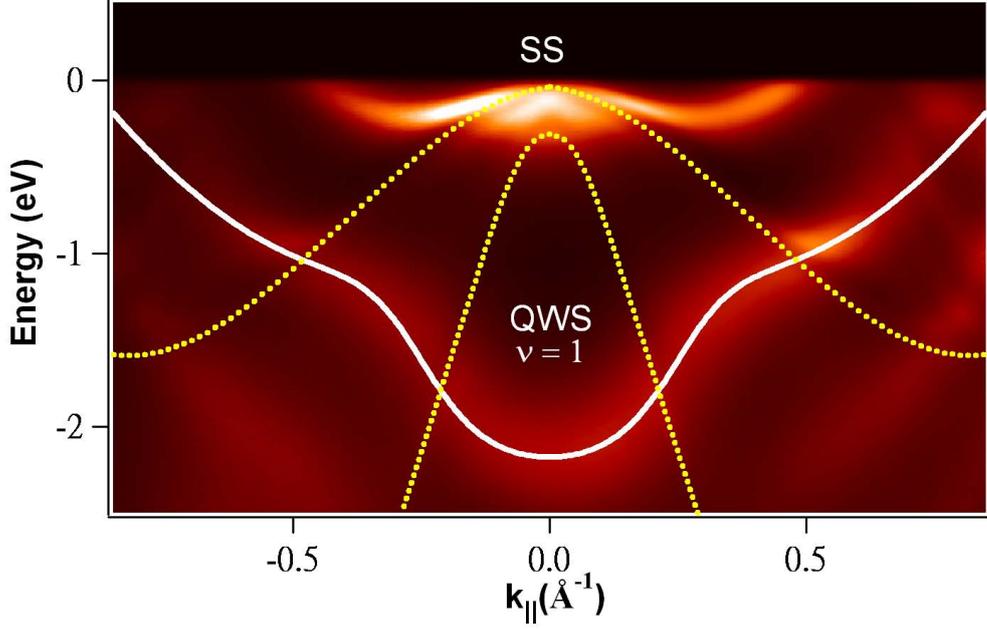
Figure 4.4: The surface state and the quantum well state dispersion are distorted near the Ge bulk band edge due to a hybridization interaction.

$$E_\nu(k_\parallel) = E_\nu(k_\parallel = 0) + \frac{\hbar^2 k_\parallel^2}{2m^*}\left(\frac{1 + ak_\parallel^2 + bk_\parallel^4}{1 + ck_\parallel^2 + dk_\parallel^4}\right) \tag{4.1}$$

where a Pade function (radio of polynomials) is employed to account for the band distortion; a, b, c, d, and the zone-center effective mass $m*$ are treated as fitting parameters.

4.4 Discussion

The dispersion relations are governed by Bohr-Sommerfeld quantization rule:

$$2k_\perp Nt + \phi = 2n\pi \tag{4.2}$$

where $k_\perp$ is the wave vector component perpendicular to the film surface, N is the film thickness in monolayers, t is the monolayer thickness, $\phi \equiv \phi(k_\perp, k_\parallel)$ is the total phase shift at the boundary, and $n = N - \nu$ is a quantum number.

The allowed $k_\perp$ determines the binding energy of a quantum well peak through the bulk band dispersion relation. Analyzing the EDC curve at normal emission,
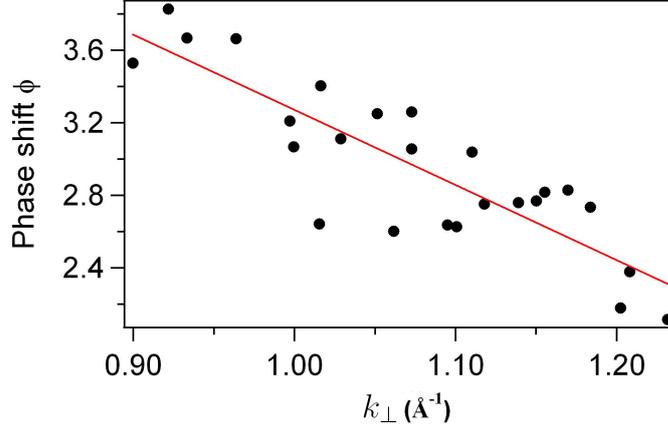
Figure 4.5: The total phase shift as a function of $k_\perp$ at $k_\parallel = 0$.

the peak positions were fit to a set of Lorenzian functions on a smooth background and the corresponding values of $k_\perp$ were obtained by the Ag bulk band calculation from Γ to L. Apply the quantization rule, the total phase shift at normal emission are calculated, shown in Fig. 4.5.

For increasing in-plane momentum, each quantum well state exhibits a dispersion relation $E_\nu(k_\parallel)$. The $k_\perp$ is dependent on $k_\parallel$ due to the quantization rule. This yields the subband dispersion through the bulk band dispersion $E(k_\perp, k_\parallel)$:

$$E_\nu(k_\parallel) = E(k_{\nu\perp}(k_\parallel), k_\parallel) \tag{4.3}$$

The zone-center effective mass of each subband is given by :

$$\frac{1}{m_\nu*} = \frac{1}{\hbar^2} \frac{d^2 E_\nu(k_\parallel)}{dk_\parallel^2} \tag{4.4}$$

When the phase shift derived from both $k_\perp$ and $k_\parallel$ dependence is taken into consideration in the quantization rule, a straightforward calculation of the zone-center effective mass are obtained

$$\frac{1}{m_\nu*} = \frac{1}{\hbar^2} \frac{\partial^2 E_\nu(k_\parallel)}{\partial k_\parallel^2} - \frac{1}{\hbar^2} \frac{\frac{\partial E}{\partial k_\perp} \frac{\partial^2 \phi}{\partial k_\parallel^2}}{2Nt + \frac{\partial \phi}{\partial k_\perp}} \tag{4.5}$$

where the first term on the right hand side of (4.5) is the inverse of the effective

44

mass in the bulk limit of $N \to \infty$; that is

$$\frac{1}{m_{bulk}} = \frac{1}{\hbar^2} \frac{\partial^2 E_\nu(k_\parallel)}{\partial k_\parallel^2}. \tag{4.6}$$

To simplify the problem, we assume the phase shift as

$$\phi(k_\perp, k_\parallel) = \phi_0(1 + Ak_\perp)(1 + Bk_\parallel^2) \tag{4.7}$$

where the only squared term of $k_\parallel$ is used for symmetry. At normal emission, where $k_\parallel$ is zero, the phase shift reduces to a linear function.

Using this model and our assumption, the effective mass can be fit by the fitting function :

$$\frac{1}{m_\nu} = \frac{1}{m_{bulk}} - \frac{1}{\hbar^2} \frac{2B\phi_0(1 + Ak_\perp)\frac{\partial E}{\partial k_\perp}}{2Nt + \phi_0 A} \tag{4.8}$$

where $\frac{\partial E}{\partial k_\perp}$ and m_{bulk} can be obtained from the calculated bulk band dispersion from Γ to L point taken from an empirical analysis of Smith et al [30].

We performed simultaneous fitting of the phase shift with k-dependence, the thickness, and energy dependence of effective mass at $k_\parallel = 0$. The numerical values of the fitting parameters are $\phi_0 = 7.42$, $A = -0.56$ and $B = 3.92$. The solid curve in Fig. 4.5 is the result from a simultaneous fitting. Combining the Bohr-Sommerfeld quantization rule and the fitting of phase shift, we obtained the theoretically expected energies of each quantum well state for all thickness at normal emission, as shown in Fig. 4.6. The fitting results are accordant to the experiment data. The outcome for effective mass are also fit well, as shown in Fig. 4.7. The small discrepancies can be attributed to inaccuracies in the band structure and the assumption of phase shift in the model. The effective mass is expected to diminish as $1/N$ for increasing film thickness. This phenomena can be explained by the Bohr-Sommerfeld quantization rule with a simple assumption that the phase shift is a function of $k_\perp$ and $k_\parallel$.
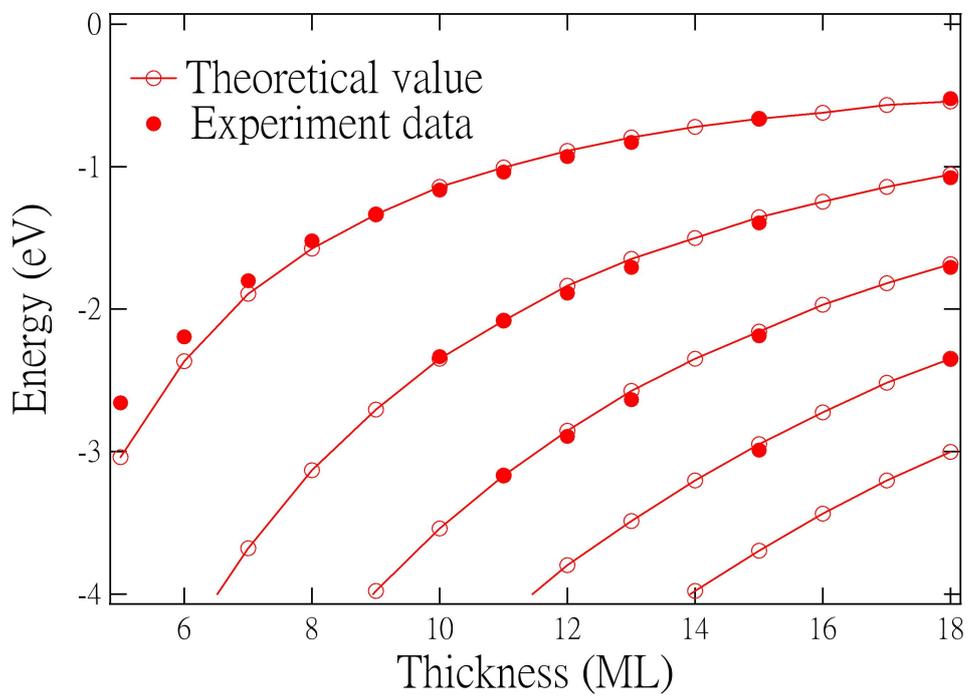
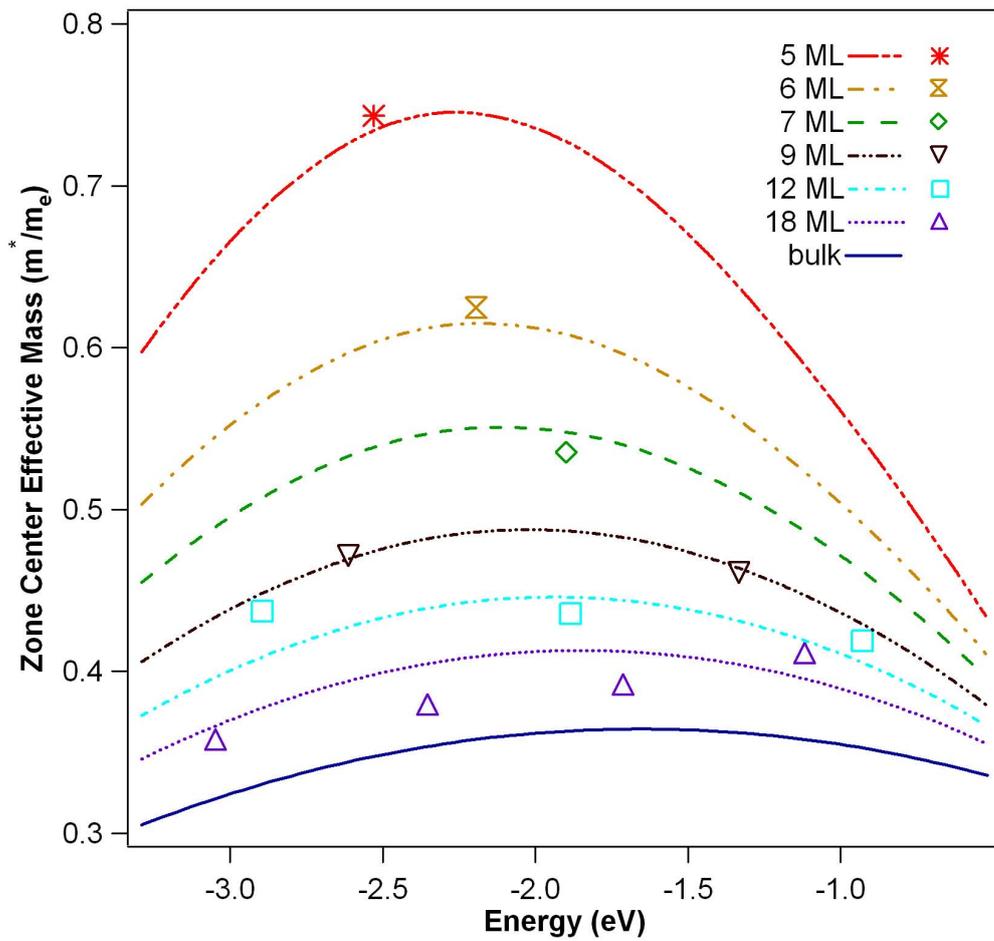Figure 4.6: Energies of quantum well resonance as a function of thickness at normal emission.

Figure 4.7: Thickness and energy dependence of the zone center subband effective mass.

Chapter 5

Submonolayer Pb on Ge(111)

Lead deposits on Ge surfaces have received a large amount attention. Pb on Ge is considered "prototypical" system for study metal/semiconductor interface. $(\sqrt{3} \times \sqrt{3})R30°$ is a common reconstruction in metal/semiconductor interface. It is stabilized by the minimization of the Ge dangling bonds. The study of the submonolayer Pb on Ge(111) was reported by many groups. When the highly-doped n-type Ge(111) are used, the electronic structures are different from those previously reported.

When Pb atoms are absorbed on highly-doped (dopant concentration of $1 \times 10^{17} \sim 1 \times 10^{18}$ cm^{-3}) n-type Ge(111), the valence band of Ge including the heavy-hole, light-hole, and split-off hole bands are reflected and probed by angle-resolved photoemission spectroscopy. The effective masses of carriers in the conduction band and valence bands near the band edges have been measured by cyclotron resonance in many semiconductors.

5.1 Experiment

The Ge(111)-$c(2 \times 8)$ was prepared by cycles of sputtering at 500°C with Ne gas, followed by annealing at 600°C. The cleanness of sample was checked by LEED pattern and photoemission spectrum.

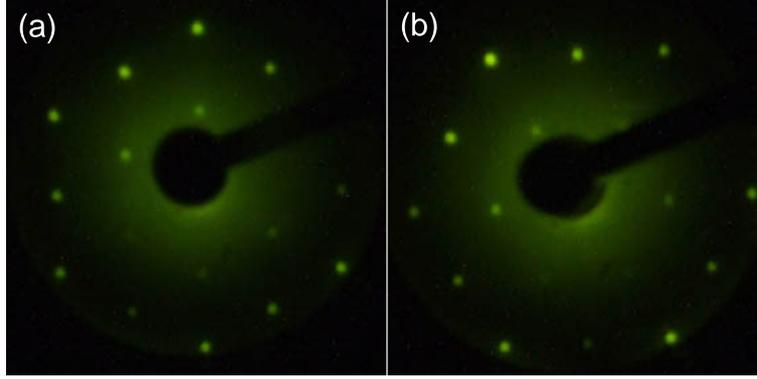2 ML of Pb (in substrate unit) was deposited by EFM3 with a rate of 0.2 ML/min

Figure 5.1: The LEED pattern of $(\sqrt{3} \times \sqrt{3})R30°$ reconstruction with electron energy 40eV.

onto the substrate at room temperature . The sample was then annealed to 200°C and a $(\sqrt{3} \times \sqrt{3})R30°$ reconstruction was formed. The LEED pattern of the $(\sqrt{3} \times \sqrt{3})R30°$ reconstruction was shown in Fig. 5.1. This reconstruction can be also obtained by deposing several monolayer Pb film at 120 K followed by annealing to 300°C. A sharp $(\sqrt{3} \times \sqrt{3})R30°$ LEED pattern can be obtained by different condition and we can conclude that the reconstruction is stable.

The dispersion relation along two symmetry directions, $\bar{\Gamma}\bar{M}\bar{\Gamma}$ and $\bar{\Gamma}\bar{K}\bar{M}$, are recorded at 120 K. The measured direction can be calibrated by LEED pattern, which reflects corresponding surface Brillouin zone (SBZ) as shown in Fig. 5.2. The dashed line represents the SBZ of Ge(111) and the solid line represents the SBZ of the $(\sqrt{3} \times \sqrt{3})R30°$ reconstruction. A photon energy of 21.2 eV (He I α) is used. The electronic structures are measured both at room temperature and low temperature (120 K).

To distinguish between bulk or surface emission bands, different photon energies are applied. In contrast to bulk state, the peak position of a surface state in photoemission spectra is independent of the photon energies used. Synchrotron radiation source provides tunable photon energies. The experiments using synchrotron radiation light source were performed on the BL21B1 beamline at NSRRC in Taiwan. This is an ultra-high resolution and high flux beamline, covering the photon energies from 5 to 100 eV. The reconstruction was obtained by the same procedure. The band dispersion were also measured along two symmetry directions with different
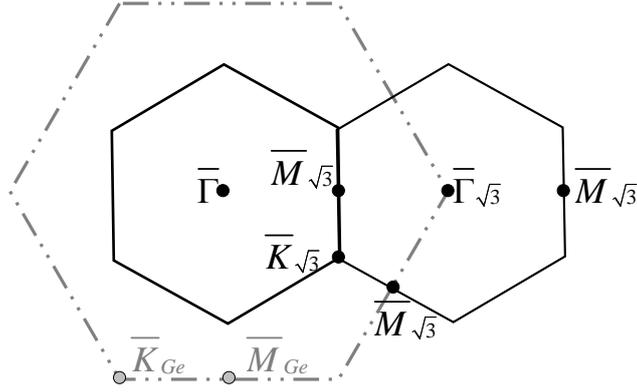
Figure 5.2: The corresponding SBZ of the $(\sqrt{3} \times \sqrt{3})R30°$ reconstruction.

photon energies.

5.2 Result

Figure 5.3 (a) and (b) show the series of energy distribution curves with increasing emission angles. Normal emission corresponds to $\theta = 0$ and the surface electronic structure can be probed from $\bar{\Gamma}$ toward to the surface zone boundary by varying $k_{\parallel}$.

Figure 5.3 (a) shows three electronic state features along $\bar{\Gamma}\bar{M}\bar{\Gamma}$ direction. These states are clearly observed and labeled as A, B, I, H1, H2 and H4. State A is observable for emission angles 19° - 26° at binding energy at 0 to 0.6 eV; state B2 is observable for emission angles 16°-30° at binding energy at ∼ 0.8 eV. A and B are combine to state I , observed at large emission angles ≥ 30°.

Figure 5.3 (b) shows the electronic state features along $\bar{\Gamma}\bar{K}\bar{M}$ direction. These states are clearly observed and labeled as C-G and h1-h2. State C is observable for emission angles 15° - 22° at binding energy ∼ 0.35 eV; state D is observable for emission angles 17°-22° at binding energy at ∼ 0.8 eV. Both E and G are symmetry to $\bar{M}$, observed at large emission angles 22°-33° and 18°-33°. State F is observable for emission angles 17° - 22° at binding energy ∼ 0.7 eV.

Dispersion relations were mapped along the $\bar{\Gamma}\bar{M}\bar{\Gamma}$ and $\bar{\Gamma}\bar{K}\bar{M}$ directions , as shown
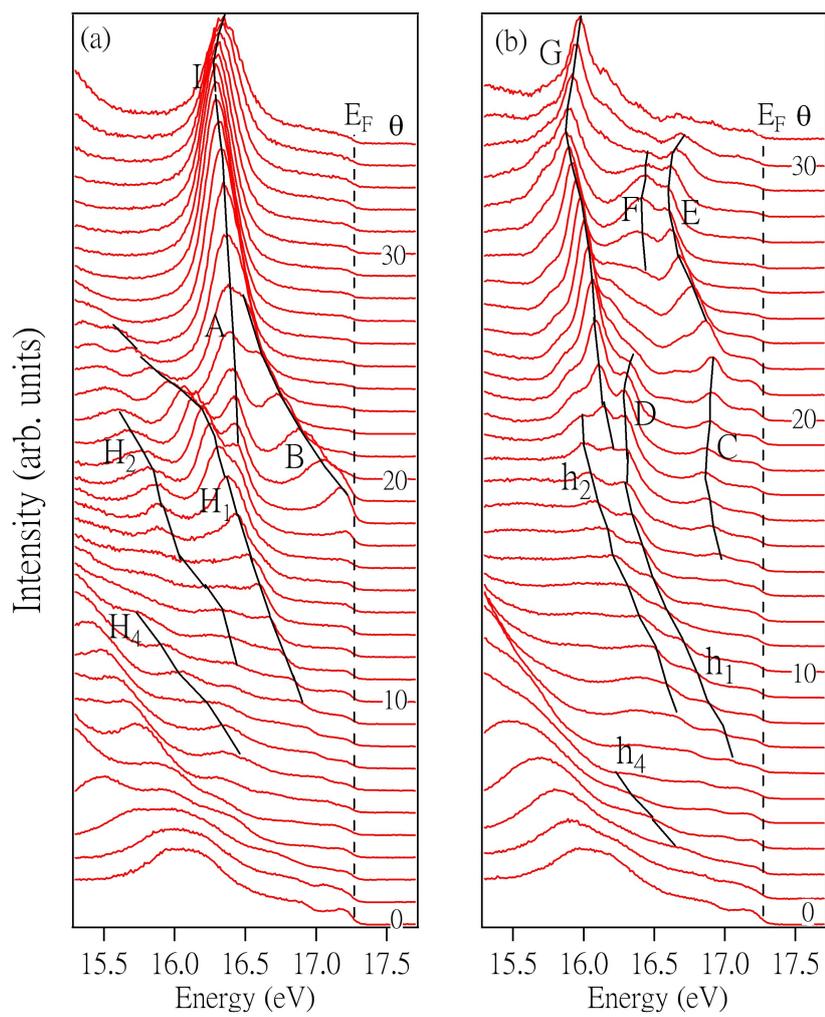
50

Figure 5.3: The EDCs along (a) $\bar{\Gamma}\bar{M}\bar{\Gamma}$ and (b) $\bar{\Gamma}\bar{K}\bar{M}$ directions.

in Fig. 5.4 and 5.5. The vertical axis is the energy, and the horizontal axis is the in-plane momentum of the photoelectron, $k_{\parallel}$, calculated from the polar emission angle. The 2D dispersion of the electron band along two symmetry directions, are measured both at room temperature and low temperature. The red vertical lines denote high symmetry points of the $(\sqrt{3} \times \sqrt{3})R30°$ unit cell. The high symmetry points in the fcc(111) surface are $\bar{M}$ and $\bar{K}$, where $\overline{\Gamma M} = \sqrt{2}\pi/(a\cos 30°)$ and $\bar{\Gamma}\bar{K} = \sqrt{2}\pi/(a\cos^2 30°)$ with lattice constant a. For the $(\sqrt{3} \times \sqrt{3})R30°$ unit cell, the distances between each symmetry point are $\bar{\Gamma}\bar{K} = 0.61$, $\bar{\Gamma}\bar{K}\bar{M} = 0.92$, $\bar{\Gamma}\bar{M} = 0.53$, and $\bar{\Gamma}\bar{M}\bar{\Gamma} = 1.06$.

The electronic states labeled in energy distribution curve (EDC) are also labeled in 2D images. Near the zone center $\bar{\Gamma}$, some electronic states with weak intensity are not noticeable in EDC's, but they are easier to see in the 2D image. The states are labeled H1-H4 and h1-h4 for the two measured directions, respectively.

The electron structure of the Pb/Ge(111)-$(\sqrt{3} \times \sqrt{3})R30°$ were reported in previous research. With angle-resolved photoemission spectroscopy (ARPES), Carlisle at $al.$ observed that the α and γ reconstructions of Pb/Ge(111) system have the same electronic structure in the two symmetry directions although their atomic structures are different. Their spectrum show that surface states cross the Fermi level and both two phase are metallic, as shown in Fig. 5.6.

The bands dispersions are very different from the previous reports. This may be caused by the substrate doping concentration (dopant concentration of 1×10^{17} - 1×10^{18} cm^{-3}). The band dispersions observed from our experiment have the feature of the $(\sqrt{3} \times \sqrt{3})R30°$ reconstruction. Along the $\bar{\Gamma}\bar{M}\bar{\Gamma}$ direction, state I is centered at the second $\bar{\Gamma}$ point around 0.9 eV. The band folding effected are observed. State B centered at the second $\bar{\Gamma}$ point and a weak feature, label as B', centered at the zone center are observed. Along the $\bar{\Gamma}\bar{K}\bar{M}$ direction, state C and D are centered at $\bar{K}$; state E and G are centered at $\bar{M}$ point. The faint feature C' observed at low temperature are centered at $\bar{K}$.
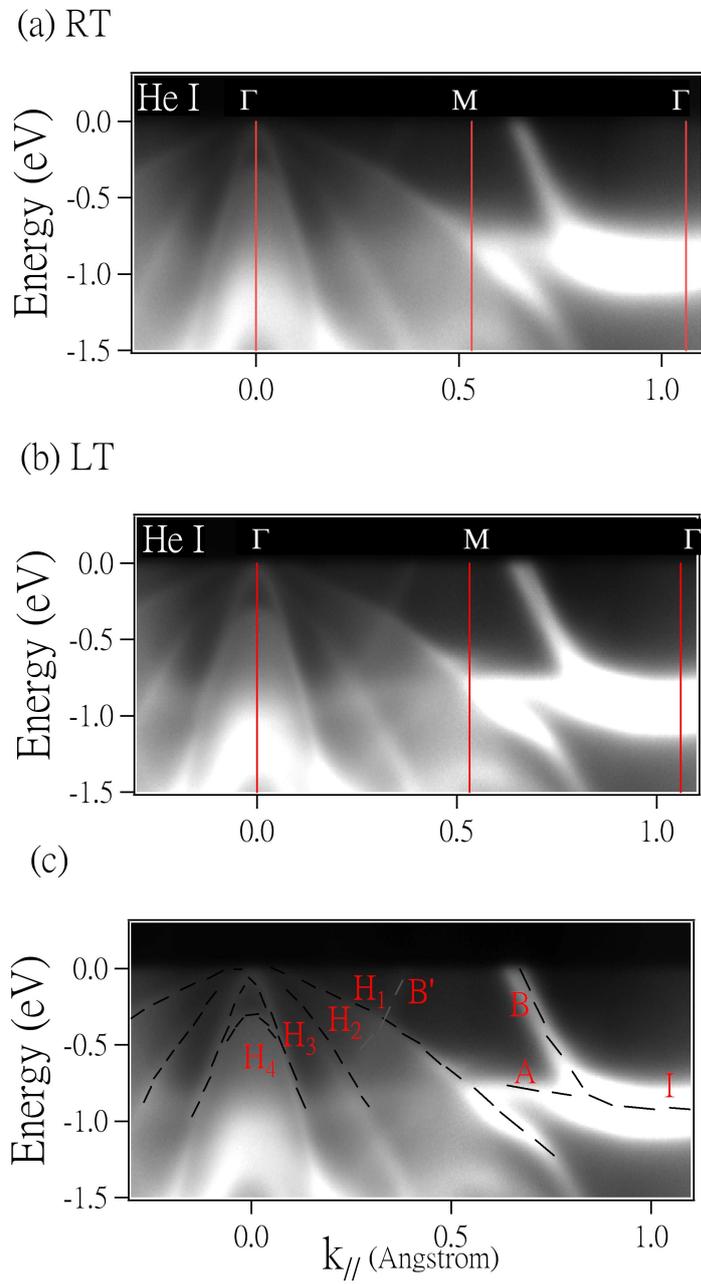
(a) RT

(b) LT

(c)

Figure 5.4: The 2D image along $\bar{\Gamma}\bar{M}\bar{\Gamma}$ direction.
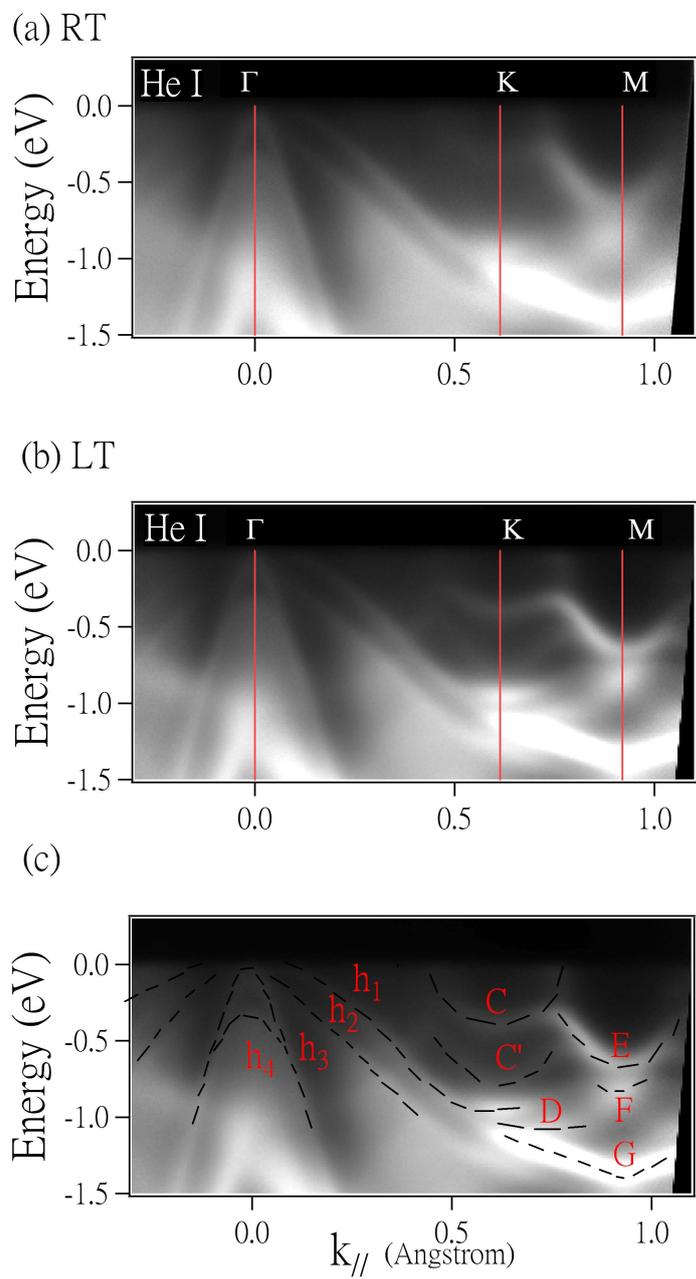
53

(a) RT

(b) LT

(c)

Figure 5.5: The 2D image along $\bar{\Gamma}\bar{K}\bar{M}$ direction.
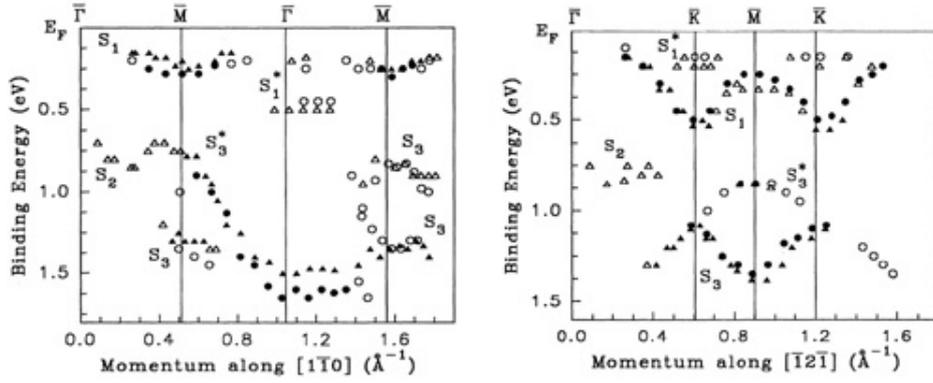
54

Figure 5.6: The energy dispersion of surface states detected along two symmetry directions with photon energy 20 eV at room temperature. [17]

5.2.1 Difference at RT and LT

Usually, measurements of photoemission spectra are done at low temperature to reduce the background and thermal broadening. The electronic states detected at room temperature and low temperature are essentially equivalent. Spectra show rather broad peaks at room temperature. As shown in Fig. 5.7 (c), the peaks of EDC at $k_\parallel = 0.65$ Å^{-1} are sharper and the peaks can be resolved at low temperature.

The main difference is the presence of the C' state along the $\overline{\Gamma K M}$ direction. Along the $\bar{\Gamma}\bar{K}\bar{M}$, a faint feature at ~ 0.6 eV close to $\bar{K}$ is observed at low temperature. This state is not easy to observe in the EDC or 2D image. Figure 5.7 shows the gradient of the 2D image from the Fig. 5.5. The EDC at $k_\parallel = 0.78$Å, shown in Fig. 5.7 (c), shows clearly that a new peak emerges at binding energy 0.6 eV.

5.2.2 2D Dispersion

To know that the electronic states are 2D or 3D states, different photon energies were applied. The band dispersion along $\bar{\Gamma}\bar{M}\bar{\Gamma}$ and $\bar{\Gamma}\bar{K}\bar{M}$ directions are measured with photon energies 17, 21, and 25 eV, as shown in Fig. 5.8 and 5.9. The features look the same as different photon energies are used.
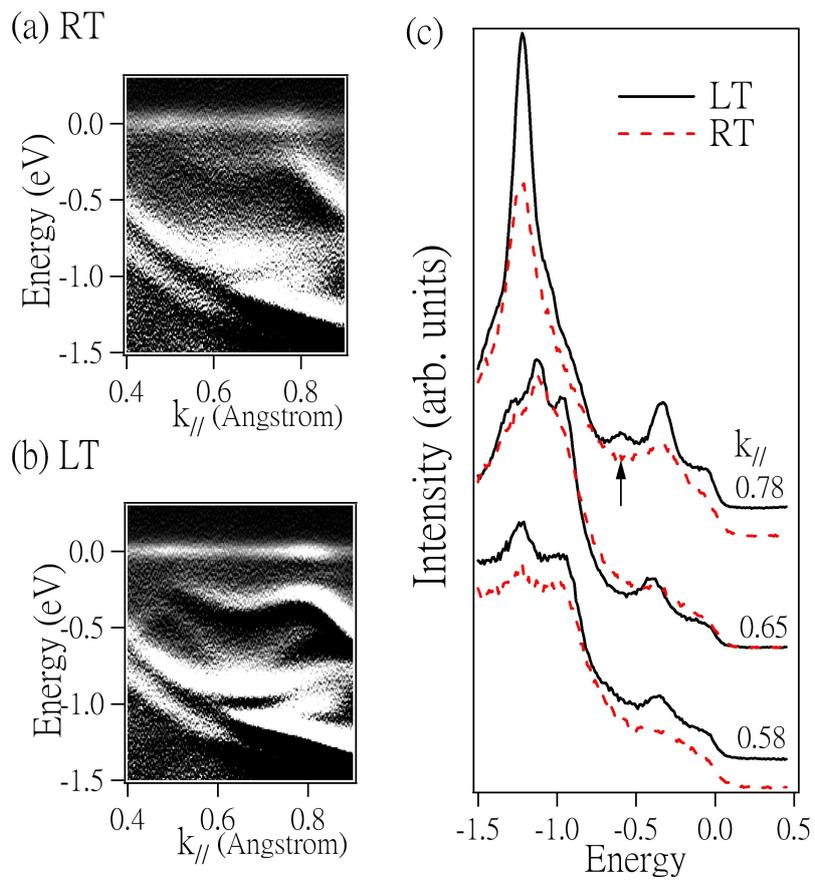
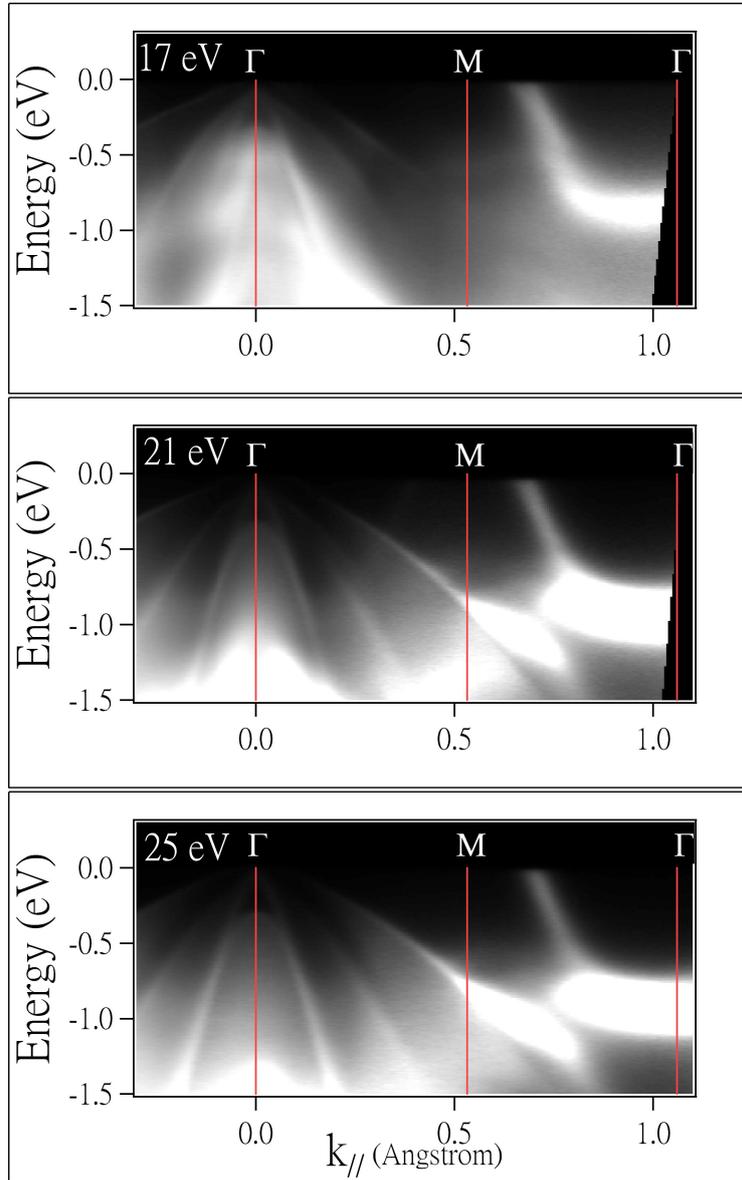Figure 5.7: A new band emerges at low temperature.

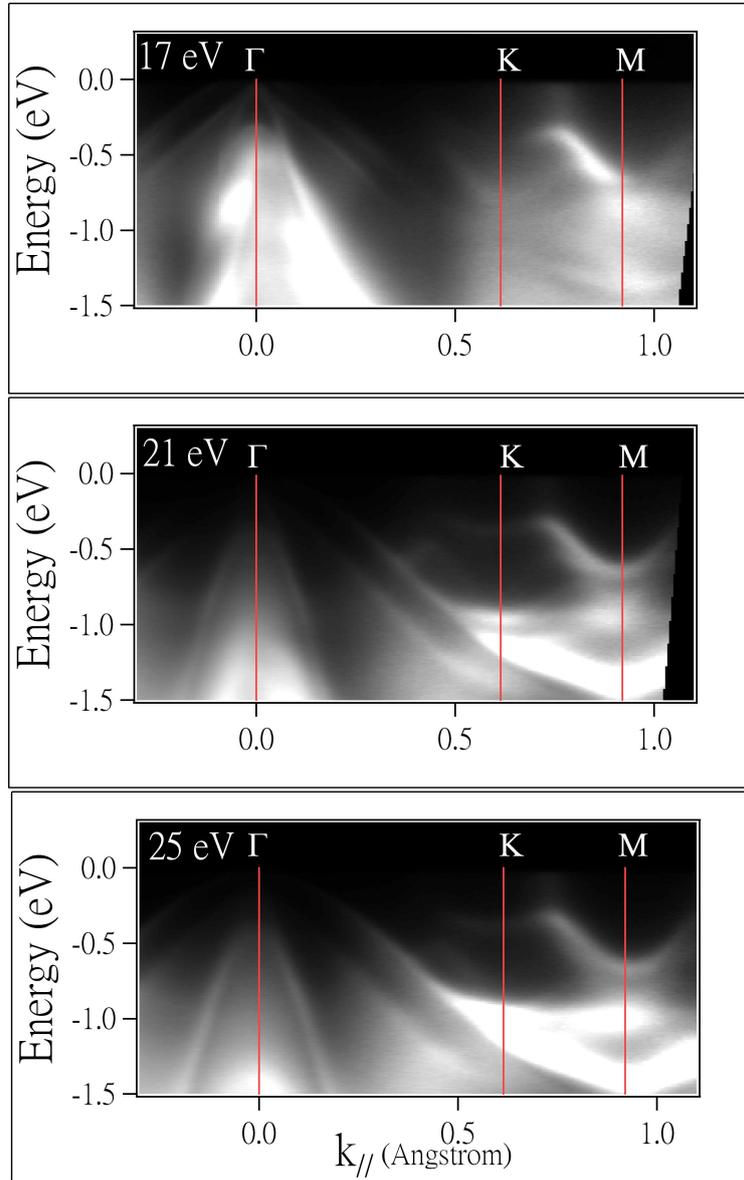Figure 5.8: The 2D image along $\bar{\Gamma}\bar{M}\bar{\Gamma}$ direction with different photon energies.

Figure 5.9: The 2D image along $\bar{\Gamma}\bar{K}\bar{M}$ direction with different photon energies.
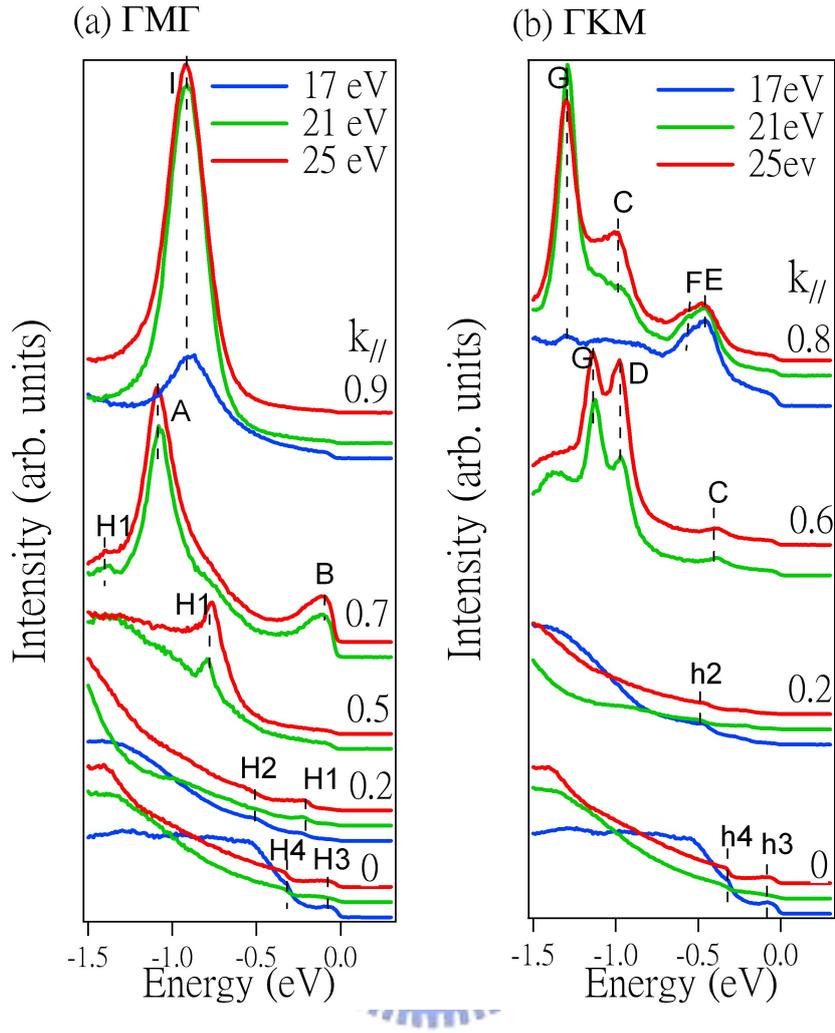
Figure 5.10: The EDCs along $\bar{\Gamma}\bar{M}\bar{\Gamma}$ and $\bar{\Gamma}\bar{M}\bar{\Gamma}$ direction with different photon energies.

Analyzing the photoemission spectra amply, the EDC curves of various photon energies are shown at varying $k_{\parallel}$. Along the $\bar{\Gamma}\bar{M}\bar{\Gamma}$ and $\bar{\Gamma}\bar{K}\bar{M}$ directions, most peak positions do not move as changing photon energies, shown as Fig. 5.10 (a) and (b). The electronic states H1-H4, h1-h4, A-I and C' are all surface states.

5.2.3 Observation of Substrate Band Edges

The interesting feature are the states near the zone center, H1-H4 and h1-h4. Their peak position did not vary with photon energies, as shown as Fig. 5.11. The central portion of the 2D image shows four concave bands, three of them corresponding well to the bulk Ge valence band edges (heavy hole, light hole, and split-off hole
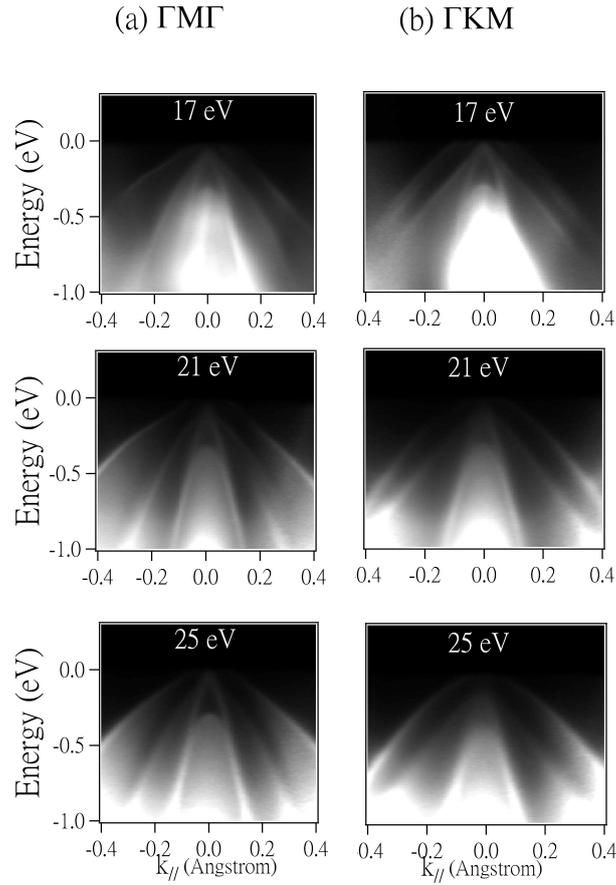
(a) ΓMΓ   (b) ΓKM

Figure 5.11: The 2D image with different photon energies.

bands). As shown in Fig. 5.12 (a), those bands detected along the $\bar{\Gamma}\bar{M}\bar{\Gamma}$ correspond well to the Ge bands along the [110] direction [31]. They match well with the bands H1, H2, and H4.

5.3 Discussion

In our experiment, a remarkable change of the electronic structure between RT and LT is that a new surface state band emerges when the temperature is cooled down. Pb/Ge(111) have been well studied. A phase transition of 1/3 monolayer Pb on Ge(111) from a room temperature $(\sqrt{3} \times \sqrt{3})R30°$ phase to a 3×3 phase below 200 K. This have been observed from LEED pattern or a STM image [32]. The angle-resolved photoemission study of the electronic structure on Pb/Ge(111) has been probed and the remarkable change is that the upper surface state is much more clearly split into two bands at LT [33]. Many explanations were proposed to explain
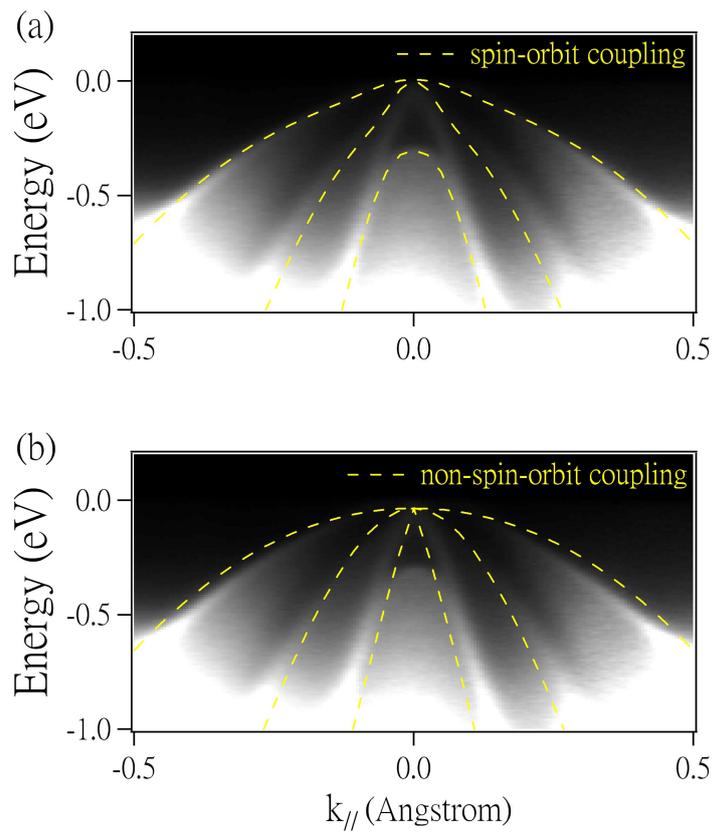
Figure 5.12: Comparison the experimental data to the calculated Ge bulk band with the (a) spin-orbit coupling and (b) non-spin-orbit coupling.
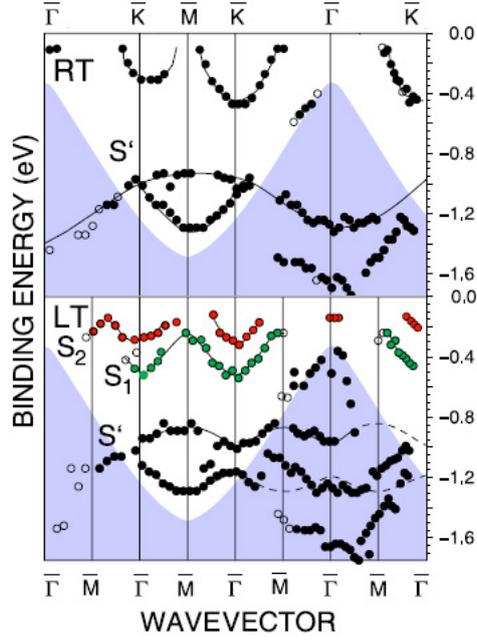
Figure 5.13: The band splitting around the $\bar{K}$ points at LT.[33] Solid lines denote high symmetry points of the $(\sqrt{3} \times \sqrt{3})R30°$ unit cell (upper panel) and 3×3 unit cell (lower panel) [33].

the phase transition, such as nesting instability, defect-mediated density waves, and dynamical fluctuations.

Mascaraque *at al.* reported the appearance of a different surface band with a 3×3 periodicity at low temperature using photons with 32 eV [33], as shown in Fig. 5.13. The band found in the vicinity of the Fermi level was detected as shoulder in the low temperature peak. The phase transition was considered to be induced by the thermal disorder and should be an order-disorder type. Maybe the structure has two kinds of Pb atoms, whose vibrational movement is stabilized at low temperature. The driving force of the phase transition in our system is not clear. The possible explanation can not be proved only on the basis of the electronic structure and the detailed information on the atomic structures of the $(\sqrt{3} \times \sqrt{3})R30°$ and 3×3 are required.

However, the LEED pattern was not observed to change in our experiment when the temperature is cooled down to 50 K, while the new surface bands centered at $\bar{K}_{\sqrt{3}}$ become resolved at low temperature. It is possible that the atomical change of

the Pb-$\sqrt{3}$ surface was not sensitive to LEED pattern.

The more interesting bands are those faint bands centered at zone center. They match well with the Ge bulk band edges (heavy hole, light hole, and split-off hole bands) from calculation.

Depending on the species and the structure of the adsorbed atoms, the surface states act as donor-type or acceptor-type states. Depending on the position of the Fermi level, donor-type surface state can carry a positive charge and acceptor-type surface state a negative charge. The charge of surface states is compensated by an opposite charge inside the semiconductor. The charge screens the surface charge is called the space charge Q_{SC} and the spatial regions of redistributed screening charges are called space charge layers. The occupied surface states induce strong band bending. Fig. 5.14 shows the band scheme for a n-type semiconductor space charge layer. Partially occupied acceptor type surface state carrying negative charge is compensated by the space charge. Bulk donor states are lifted above the Fermi level and are empty of electrons. The exact position of Fermi energy at the surface is determined by charge neutrality. The distribution of space charge is related to the curvature of the electronic bands. Due to the band bending, free electrons are pushed away from the surface and their density is lowered. This space charge layer is called a *depletion layer*. Higher density of acceptor surface states at lower energies in the band gap can induce stronger upward band bending. The space charge layer extends deeper into the semiconductor and the band bending is stronger that the intrinsic energy crosses the Fermi energy. This space layer is called a *inversion layer*.

Pb atoms adsorbed on Ge surface form an ordered structures and create surface states in the band gap. The surface states of the $(\sqrt{3} \times \sqrt{3})R30°$ reconstruction on normal doped Ge(111) consists of upward parabolic bands. If the surface states are acceptor-type and carry negative charge, which is screened by an opposite charge inside the semiconductor. Electron occupation in the surface states induce strong upward band bending. The surface states can penetrate into the bulk and the interaction of the surface states and the Ge bulk band in the inversion layer are
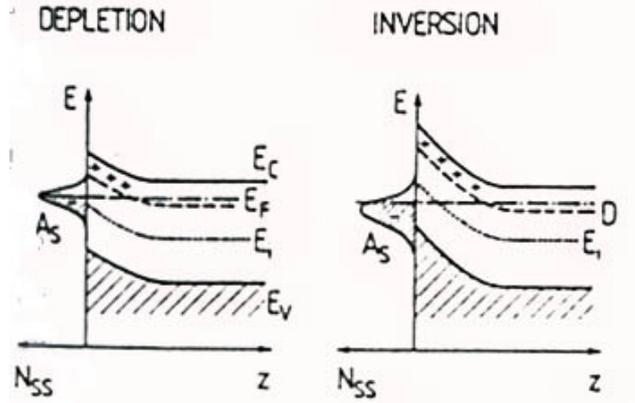
Figure 5.14: Bans scheme of a (a) depletion and (b) inversion space charge layer on a n-type semiconductor [2].

considered. Near the zone center, the surface states occupation in (E, k) diagram is coincident with the Ge bulk band, leading to the strong interaction between the surface state and Ge bulk bands. Due to the fact that Ge bulk continuum dominates the density state, the surface state band reflects the Ge bulk band edge as a result of strong interaction.

The surface bands H1, H2, and H4 can be well explained by the surface bands inducing space charge layer. We compare the non-spin-orbit coupling Ge bands with it. They match well. The result suggests that Ge bands form spin-orbit and non-spin-orbit coupling coexists.

The band gap of Ge is an inverted gap, where the gap is p-like at the bottom and s- like at the top. Surface state derived from the conduction band are more s-like. The valence band edge of Ge is derived from $p_{\frac{3}{2}}$ and $p_{\frac{1}{2}}$ states of free atoms. There are no bands splitting off from the s-type band by the spin-orbit interaction. A strong interaction between p-type Ge band edges and the s-like surface band may broke the symmetry of p-type Ge band. Therefore, the spin-orbit splitting and non-spin-orbit splitting bands coexist.

Chapter 6

Conclusion

The electronic structures of the ultrathin metal films on the semiconductor have been investigated by high resolution angle-resolved photoemission. The electronic structures of Ag/Ge(111) and Pb/Ge(111) are studied.

Atomically uniform Ag film on Ge(111) were prepared at the thickness ranging 5-18 monolayers. A detailed investigation of the subband dispersion relations in Ag films of various thickness deposited on Ge(111) is probed by angle-resolved photoemission. The effective mass at the zone center were extracted through a fitting model of a Pade function.

That effective masses at the zone center of subbands for the Ag/Ge(111) were found to increase with decreasing thickness. The effective mass at the zone center of each subband is coupled to the $k_\parallel$ dependence of $k_\perp$ for the quantum well state band structures due to the Bohr-Sommerfeld quantization rule. This behavior is simply caused by a boundary effect through both $k_\perp$ and $k_\parallel$ momentum dependent phase shift.

Submonolayer Pb film deposited on Ge(111) results in $(\sqrt{3} \times \sqrt{3})R30°$ reconstruction. The electronic structures are probed both at room temperature and low temperature. A new surface state band centered at $\bar{K}_{\sqrt{3}}$ emerges at $T = 120$ K while no phase transition is observed by LEED pattern.

The electronic structures are different from the previous report. The surface state band dispersion reflects the Ge bulk band edges, including the heavy-hole, light-hole, and split-off hole bands. We propose that a space charge layer is induced on the highly-doped n-type Ge(111) surface by a Pb-induced acceptor type surface state, resulting large band bending and strong hybridization interaction between the surface state and the Ge substrate bands. It is the first time observation that spin-orbital splitting and non-spin-orbital splitting bands coexist at the interface of metal/semiconductor.

Bibliography

[1] Stefan Hüfner, *Photoelectron Spectroscopy*, Springer

[2] Hans Lüth, *Surfaces and Interfaces of Solid Materials* , Springer

[3] G Schönhense, and U Heinzmann, *J. Phys. E: Sci. Inst.* **16**, 74 (1983)

[4] P. S. kirchmann, M. Wolf, J. H. Dil, K. Horn, and U. Bovensiepen, *Phys. Rev. B.* **76***, 075406* (2007)

[5] K. Horn, B. Reihl, A. Zartner, D. E. Eastman, K. Hermann, and J. Noffke, *Phys. Rev. B.* **57***, 14758* (1998)

[6] *http://www.nsrrc.org.tw/english/lightsource.aspx* , NSRRC

[7] *User Manual SCIENTA R3000* , VG SCIENTA

[8] Peter Y. Yu and Manuel Cardona, *Fundamentals of Semiconductors*, Springer

[9] *http://cst-www.nrl.navy.mil/bind/static/index.html*

[10] J. J. Métois and G. Le Lay, *Surf. Sci.* **133***, 422* (1983)

[11] G. Le Lay and J. J. Métois, *Appl. Surf. Sci.* **17***, 131* (1983)

[12] T. Ichikawa, *Solid State Commun* **46***, 827* (1983)

[13] T. Ichikawa, *Solid State Commun* **49***, 59* (1983)

[14] R. Fiedenhans'l, J. S. Pedersen, M. Nielsen, F. Grey, and R. L. Johnson, *Appl. Surf. Sci.* **178***, 927* (1986)

[15] H. Huang, C. M. Wei, H. Li, B. P. Tonner and S. Y. Tong, *Phys. Rev. Lett.* **62***, 559* (1989)

[16] J. A. Carlisle, T. Miller, and T. C. Chiang, *Phys. Rev. B.* **47**, *3790* (1993)

[17] J. A. Carlisle, T. Miller, and T. C. Chang, *Phys. Rev. B.* **47**, *10342* (1993)

[18] S. A. de Vries, P. Goedtkindt, P. Steadman, and E. Vlieg, *Phys. Rev. B.* **59**, *13301* (1999)

[19] E. Ganz, F. Xiong, Ing-Shouh Hwang, and J. Golovchenko, *Phys. Rev. B.* **43**, *7316* (1991)

[20] R. D. Bringans, and H. Höchst, *Phys. Rev. B.* **25**, *1081* (1982)

[21] J. Aarts, A. J. Hoeven, and P. K. Larsen, *Phys. Rev. B.* **37**, *8190* (1988)

[22] A. R. Smith, K. J. Niu, C. K. Shih, *Science* **273**, *226* (1996)

[23] M. H. Upton, T. Miller, and T. C. Chiang, *Appl. Phys. Lett.* **85**, *1235* (2004)

[24] T. Valla, P. Pervan, A. B. Hayden, and D. P. Woddruff, *Phys. Rev. B.* **54**, *11786* (1996)

[25] Y. Z. Wu, C. Y. Won, E. Rotenberg, H. W. Zhao, F. Toyoma, N. V. smith, and Z. Q. Qiu, *Phys. Rev. B.* **66**, *245418* (2002)

[26] P. D. Johnson, K. Garrison, Q. Dong, N. V. Smith, Dongqi Li, J. Mattson, and S. D. Bader, *Phys. Rev. B.* **50**, *8954* (1994)

[27] M. H. Upton, T. Miller, and T. C. chiang, *Phys. Rev. B.* **71**, *033403* (2005)

[28] J. H. Dil, J. W. Kim, Th. Kampen, and K. Horn, *Phys. Rev. B.* **73**, *161308* (2006)

[29] I. B. Altfeder, D. M. Chen, and K. A. Matveev, *Phys. Rev. Lett.* **80**, *4898* (1998)

[30] N. V. Smith, *Phys. Rev. B.* **9**, *1365* (1974)

[31] U. Schmid, N. E. Christensen, and M. Cardona, *Phys. Rev. B.* **41**, *5919* (1990)

[32] Joseph M. Carplinelli, Hammo H. Weitering, E. Ward Plummer, and Roland Stumpf *Nature* **381**, *384* (1996)

[33] A. Masacaraque, J. Avila, E. G. Michel, and M. C. Asensio, *Phys. Rev. B.* **57**, *14758* (1998)